J. Fluid Mech. (2019), *vol.* 881, *pp.* 1010–1047.
doi:10.1017/jfm.2019.786

Space–time formation of very-large-scale motions in turbulent pipe flow

Jae Hwa Lee[1,3,†], **Hyung Jin Sung**[2] **and Ronald J. Adrian**[3]

[1]Department of Mechanical Engineering, UNIST, 50 UNIST-gil, Ulsan 44919, Korea

[2]Department of Mechanical Engineering, KAIST, 291 Daehak-ro, Yuseong-gu, Daejeon 34141, Korea

[3]School for Engineering of Matter, Transport and Energy, Arizona State University, Tempe, AZ 85287-6106, USA

(Received 6 May 2019; revised 10 August 2019; accepted 22 September 2019; first published online 25 October 2019)

We examine the origin of very-large-scale motions (VLSMs) in fully developed turbulent pipe flow at friction Reynolds number, $Re_\tau = 934$, using data from a direct numerical simulation. The VLSMs and the packet-like large-scale motions (LSMs) found in this study are very similar to those found in earlier studies. Three-dimensional time-evolving instantaneous fields show that one component of the process leading to the large streamwise length of VLSMs is the concatenation of adjacent streamwise LSMs caused by the continuous elongation of LSMs due to the strain component of the mean shear. Spatial organization patterns of the VLSMs and LSMs and their properties are studied by separating auto-correlation of the streamwise velocity fluctuations into the components of the VLSM and the LSM defined by low-pass/high-pass filtering in the streamwise direction. The structures of the two-point spatial correlations of the streamwise velocity component of the VLSMs and the LSMs in the streamwise-azimuthal plane are characterized by multiple maxima and complex patterns that beg explanation in terms of patterned coherent arrangements of the LSMs. Using proper orthogonal decomposition (POD), it is found that the X-shape correlation pattern of the VLSMs results from the superposition of very long helically inclined structures and streamwise-aligned structures. Further explanation of the patterns in the correlations of the VLSMs and LSMs is provided through the study of synthetically constructed arrangements of simple hairpin packet models of the LSM. Head-to-tail alignment of the model packets along streamwise and helical directions suggested by the eigenvalues of the POD creates a pair of long roll-cells centred above the logarithmic layer, and bracketing the LSMs. These roll-cells are pure kinematic consequences of the induction within the LSM packets, but they may also serve to organize smaller packets.

Key words: boundary layer structure, turbulent boundary layers

1. Introduction

Experimental and numerical studies have shown that structures with large scales and very large scales in the outer layer play a crucial role in generating and transporting

† Email address for correspondence: jhlee06@unist.ac.kr

turbulent kinetic energy and Reynolds shear stress in canonical, wall-bounded turbulent flows, such as boundary layers, pipe flows and channel flows. Falco (1977) first identified large-scale motions (LSMs) as a generalization of the bulges in the turbulent/non-turbulent interface that were known to occur at the edge of turbulent boundary layers (Kovasznay, Kibens & Blackwelder 1970; Brown & Thomas 1977), wakes and jets. Internal wall flows such as channels and pipes also contain LSMs (Liu, Adrian & Hanratty 2001), although the confinement presented by internal flows suggests that they may have to occur in patterns, in order to make room for others in the region of the centreline. Correlation measurements in boundary layers (Kovasznay *et al.* 1970) indicate that their average dimensions in the streamwise and spanwise directions are $1.5R$–$3R$ and $0.5R$, respectively, where R is used to represent the boundary layer thickness, pipe radius or channel half-height. Being the tallest structures, LSMs were defined originally by their height, not their length or width; but, in recent years they have also been defined in terms of their length or their wavelength. Following Guala, Hommema & Adrian (2006), we shall nominally take the longest wavelength of LSMs to be πR.

In contrast to LSMs, the very-large-scale motions (VLSMs) found by Kim & Adrian (1999) in turbulent pipe flow are as long as $10R$–$20R$, and since then even longer structures, up to $50R$, have been observed (Priymak & Miyazaki 1994; Hites 1997; Guala *et al.* 2006). Subsequent studies have shown that VLSMs are relatively short in boundary layers, approximately $7R$, while their mean lengths in channel flows are intermediate (Kim & Adrian 1999; Ganapathisubramani, Longmire & Marusic 2003; Guala *et al.* 2006; Balakumar & Adrian 2007; Hutchins & Marusic 2007*a*; Dennis & Nickels 2011; Lee & Sung 2011; Wu, Baltzer & Adrian 2012). (See also Bullock, Cooper & Abernathy (1978) whose observations of very long modes in fully turbulent pipe flow may be the earliest made.) Adrian (2007) and Marusic *et al.* (2010) review aspects of these interesting structures.

Hairpin packets consist of a coherent group of hairpin vortices aligned more or less along the streamwise direction (Zhou *et al.* 1999; Adrian, Meinhart & Tomkins 2000). Zhou *et al.* (1999) found that single hairpins whose strengths (defined as the maximum induced velocity relative to the mean flow) exceed a threshold value generate new hairpin vortices upstream and downstream of the primary vortex. They explained this phenomenon 'on the basis of the delicate balance between self-induced and mutually induced motion of the quasi-streamwise vortex legs which tend to lift the vortices up and back, and the influence of mean shear which stretches and intensifies the vortices along the streamwise direction'. In addition, Adrian *et al.* (2000) showed that the flow in a boundary layer is the combination of packets having various ages and sizes in a hierarchy of scales that increase with distance from the wall. The coherent vortex packets that originate close to the wall frequently occur within the relatively uniform, low-momentum zones inside larger, faster moving packets (Meinhart & Adrian 1995). In turn, the larger low-momentum zones may be the induced interior flow of still older packets of coherently aligned vortices that originate upstream and overrun the younger, more recently generated packets. The number of low-momentum zones in the hierarchy is presumably proportional to the von Kármán number of the flow. The largest, outermost hairpin packets in the hierarchy resemble the LSMs, but differences in the growth angles suggest that another outer motion modifies the LSMs near the wall. Hairpin packets have been shown to contribute 25 % of the Reynolds shear stress while occupying less than 4.5 % of the total area (Ganapathisubramani *et al.* 2003; Lee & Sung 2011).

The existence of VLSMs was first observed in the pre-multiplied one-dimensional spectra associated with the streamwise velocity fluctuations measured by hot-wire

and using Taylor's frozen field hypothesis (Kim & Adrian 1999; Guala *et al.* 2006; Balakumar & Adrian 2007). Kim & Adrian (1999) examined the pre-multiplied spectra of a turbulent pipe flow at $y^+ = 132$ and interpreted them as bi-modal distributions with two maxima that indicated the mean wavelengths associated with VLSMs and LSMs. Guala *et al.* (2006) and Balakumar & Adrian (2007) proposed criterion for distinguishing between VLSMs and LSMs based on the streamwise lengths of the structures. Based on the crossover in co-spectra of the streamwise and wall-normal velocity fluctuations and the minimum between the VLSM and LSM spectral peaks, they defined the nominal boundary separating VLSMs from LSMs to be $k_xR = 2$, where k_x is the streamwise wavenumber. However, in view of the bi-modal interpretation of the spectra, the two modes overlap, and the VLSM cannot really be separated from the LSM by a sharp spectral cut. More properly, the nominal streamwise wavelength $\lambda_x = \pi R$ should be interpreted as the centre of a transition zone from large to very large.

The contributions of the VLSMs to the Reynolds stresses in pipe flow have been determined by integrating the energy spectra (Guala *et al.* 2006; Balakumar & Adrian 2007; Wu *et al.* 2012). The direct numerical simulation (DNS) study of Wu *et al.* (2012) in a turbulent pipe flow reported that VLSMs of wavelength greater than $3R$ contribute over 40 % of the streamwise turbulent energy, and more than 30 % of the Reynolds shear stress. These values are somewhat lower than thermal anemometer experimental results of Guala *et al.* (2006), although the difference might be due to the discrepancy in Reynolds numbers. Temporal spectra of the time series from thermal anemometer probes are necessarily converted to wavenumber spectra by using Taylor's frozen field hypothesis, commonly with the assumption that all eddies convect at the mean velocity. This procedure has been shown to amplify the long wavelength peak of the energy spectrum, raising the suspicion that the fraction of energy at longer wavelength may be overemphasized in experiments relative to the DNS (del Álamo & Jiménez 2009; Wu *et al.* 2012). On the other hand, the amplification results from the energy of long wavelengths being aliased into shorter wavelengths around the low-wavenumber spectral peak, so evaluation of the total energy contained in the VLSM range may be underestimated.

In turbulent boundary layers, streamwise velocity structures having very long lengths were first visualized experimentally by Hutchins & Marusic (2007*a*) by using a spanwise rake of 10 hot-wires and Taylor's hypothesis. They described VLSM, or 'superstructures', as they called them, in the form of very long, meandering positive and negative streamwise velocity fluctuations having individual streamwise lengths up to $\sim 20R$ in the logarithmic layer. They showed that the dominant meandering behaviour of the structures induces an X-shaped pattern in the two-point spatial correlation that changed from positive to negative values at streamwise spatial separation $\approx 3.5R$. In a DNS of turbulent pipe flow at $Re_\tau = 685$, Baltzer, Adrian & Wu (2013) also found that the pattern of the correlation contours at lower levels has a distinctive X-shape in the streamwise-azimuthal (spanwise) correlation plane. However, using conditional averages given low-momentum events, they showed that the X-shape is due to the streamwise-aligned LSMs with spanwise-offset that concatenate along dominant helix angles of 0° and 4°–8° relative to the streamwise direction. The apparent wavering of the resulting VLSM on a scale of $O(6R)$ was interpreted to be a consequence of spanwise-offset LSMs rather than a sinusoidal perturbation of an otherwise straight, streamwise-aligned sequence of LSMs. Although the very long structures in the logarithmic layers of turbulent pipe and channel flows appear to be qualitatively similar to those in boundary layer flow, some structural differences

are to be expected in the wake regions of internal and external flows (Balakumar & Adrian 2007; Monty *et al.* 2007, 2009; Lee & Sung 2013). The VLSM energy in internal flows resides both in longer wavelengths and farther from the wall than in boundary layer flow, and the streamwise wavelength of the VLSMs in the internal flows continues to increase above the logarithmic layer, while in boundary layers it does not. Because of these differences, Hutchins & Marusic (2007*a*) and Monty *et al.* (2007) used the term 'superstructures' to distinguish the very long motions in boundary layers from the VLSMs of the internal flows.

Discriminating between LSMs and VLSMs is not simple. In some studies the term 'large-scale' encompasses both the LSMs and VLSMs (Hutchins & Marusic 2007*b*; Mathis, Hutchins & Marusic 2009; Chung & McKeon 2010), perhaps, because the limited field-of-view of particle image velocimetry (PIV) could not resolve the VLSMs (Adrian 2007). It is sometimes stated that the spatial characters of the LSMs and VLSMs are similar, except for their length scales (Hutchins & Marusic 2007*a*). On the other hand, the works of Bailey *et al.* (2008) and Bailey & Smits (2010) described clear differences between the spanwise structure of VLSMs and LSMs in turbulent pipe flow, based on two-point measurements using a pair of hot-wire probes offset by various azimuthal length separations and radial positions, with varying the Reynolds number. They identified VLSM and LSM by performing cross-spectral analysis as a function of streamwise wavenumber (using Taylor's hypothesis) and azimuthal separation. Bailey *et al.* (2008) found that the azimuthal scale at streamwise wavenumbers in the VLSM range is larger than the scale for streamwise wavenumbers in the LSM range at all wall-normal distances from the wall. They noted that the difference between the azimuthal scales of VLSMs and LSMs suggests the possibility that LSMs and VLSMs could be independent entities, with VLSMs possibly arising from linear or nonlinear instabilities (del Álamo & Jiménez 2006; McKeon & Sharma 2010; Hwang & Cossu 2010).

In the present study, DNS data from the turbulent pipe simulation at $Re_\tau = 934$ by Lee & Sung (2013) is investigated to further illuminate how VLSMs are created. Baltzer *et al.* (2013) showed that VLSMs consist of LSMs concatenated to create very long structures, and Lee & Sung (2011) went further to show that streamwise stretching of the LSMs leads to the head of upstream LSM meeting the tail of downstream LSM, and concatenating by merger. However, the mechanisms causing both the organization of the LSMs and the concatenation of the LSMs are still not completely understood. For example, why are the LSMs aligned closely enough to encounter each other in the first place? Is there an unknown mechanism that brings LSMs into alignment close enough to collide as they grow longer?

To determine matters of causation, it is essential to observe the VLSMs and the LSMs in time as well as space. In § 3, three-dimensional (3-D) time-evolving instantaneous flow fields are scrutinized to provide a simple dynamical mechanism for a VLSM to form from LSMs, and in § 4, statistical properties of VLSMs and LSMs are analysed after they are separated from each other by spectral filters in the streamwise direction. Patterns of spatial organization in the two-point spatial correlations and the proper orthogonal decompositions (PODs) of the VLSMs and LSMs are used to infer aspects of the spatial organization of individual LSMs. In § 5, a model of LSMs based on various organized patterns of synthetic packets of hairpins constructed in the spirit of the hairpin vortex model of Perry & Chong (1982) is used to show that the complicated behaviour of the correlations and PODs of both VLSM and LSM can be explained by a very simple pattern. Although Townsend's attached eddy model with randomly distributed hairpin-type vortices on the wall

in a hierarchy manner has shown good prediction of the velocity statistics beyond second-order moments and spectra (Perry & Marusic 1995; Marusic & Monty 2019), there still remains the question of how they are organized in a flow field. Our model can provide a hint for how the attached structures are organized, and for how they contribute to form the patterns of the correlations, although the analysis is confined to the logarithmic layer.

2. Numerical method

The governing equations in cylindrical coordinates for incompressible, fully developed turbulent pipe flow were integrated in time using the fractional step method along with the implicit velocity decoupling procedure. Position is denoted by $\boldsymbol{x} = (x, r, \theta) = (x, y, z)$, where; x is the streamwise (or axial) distance from the inlet; r is the distance from the centreline; θ is the azimuthal angle; $y = R - r$ is the distance from the wall; and $z = r\theta$ is the spanwise distance. The corresponding velocity fluctuating components are u $(= u_x)$, v $(= -u_r)$ and w $(= u_\theta)$, and U is the temporally and spatially averaged (i.e. x- and θ-directions) streamwise mean velocity. The maximum velocity of the fully developed laminar profile (U_c) and the pipe radius (R) were used to non-dimensionalize the equations in the numerical solution. Consequently, the unit time scale is R/U_c. As usual, the superscript $+$ refers to quantities normalized by the friction velocity, u_τ or viscous length scale ν/u_τ, and the Reynolds number $Re_D = U_b D/\nu$ $(= U_c R/\nu)$ is defined based on the pipe diameter, $D = 2R$, and the bulk velocity, U_b. Numerically, $Re_D = 35\,000$, and the von Kármán number is $R^+ = Re_\tau = u_\tau R/\nu = 934$. The streamwise domain was made $30R$ long, based on the previous experimental and numerical studies of Kim & Adrian (1999) and Wu *et al.* (2012). The finite-difference grid size employed in the current work is $4097 \times 301 \times 1025$ along the axial, radial and azimuthal directions with grid resolutions $\Delta x^+ = 6.84$, $\Delta(R\theta)^+ = 5.73$, $\Delta r^+_{min} = 0.33$ and $\Delta r^+_{max} = 9.24$. The inflow and outflow conditions were periodic, and the bulk velocity was fixed leaving the integrated wall shear stress to fluctuate. Further numerical details may be found in Lee & Sung (2013).

3. Time-evolving instantaneous fields

The primary question in the present study is how a VLSM is created in the flow. The idea that small scales organize to create larger scales is quite reasonable, and it has received increasing support over the past decade (Adrian 2007). The hairpin packet model, which consists of hairpin vortices aligned in a streamwise linear fashion offers an explanation for the most fundamental features of wall turbulence, such as the multiple second quadrant bursting process, sweeps, the growth of length scale with increasing distance from the wall, and the occurrence of low-momentum zones (Meinhart & Adrian 1995; Adrian *et al.* 2000; Adrian 2007). Further, the creation of the first generation of hairpin packets in the region above the buffer layer, as explained by the auto-generation mechanism (Zhou *et al.* 1999), is an established mechanism in which hairpins with sufficient strength create more new hairpins, and so on, ultimately forming relatively coherent packets. Evidence from prior investigations (Marusic & Adrian 2012) supports the idea that the tall low-momentum zones identified as LSMs (in their figures 2–4) are among the oldest and largest packets that result from a hierarchy of streamwise and spanwise mergers starting with the first generation of packets auto-generated above the buffer layer. They are the analogues of bulges found in turbulent boundary layers.

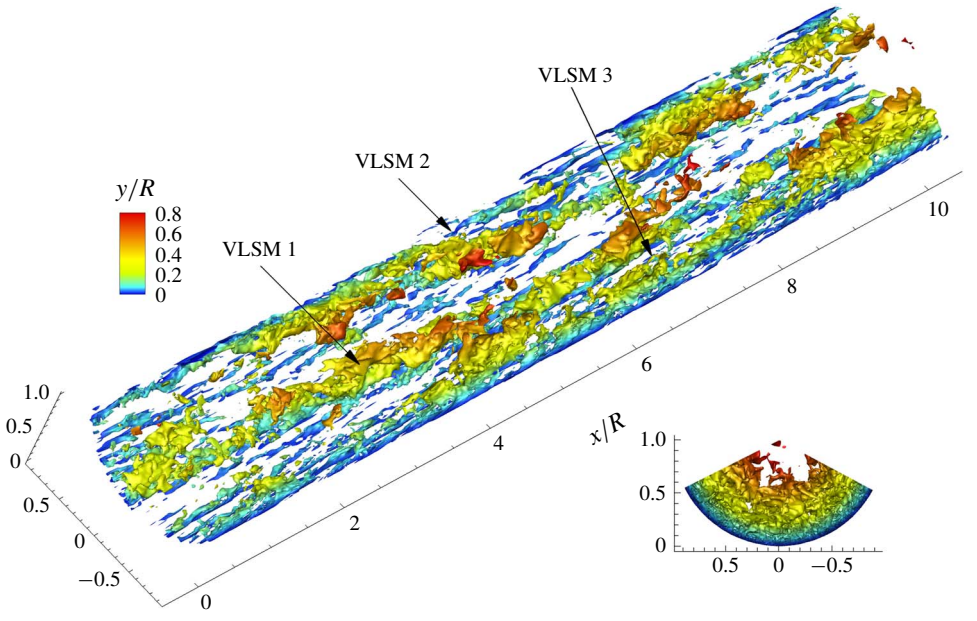

FIGURE 1. (Colour online) Three-dimensional isocontour of the streamwise velocity fluctuating structures with the contour level of $u^+ = -2$. The flow direction is from left to right. The isosurfaces are coloured based on the local value of y/R with higher y/R represented in red.

A hairpin induces negative velocity (with respect to the hairpin) in the region under its head and between its neck and legs. Inside a packet of hairpins a long low-momentum zone is formed owing to the in-line alignment of the hairpins. The ramp-shape of the low-momentum zone mimics the shape of the envelope of the hairpin packet, albeit in a smoothed manner, and it is recognized readily because the height of the envelope increases in the downstream direction along a characteristic ramp angle in the range 10°–15° (pertaining to the logarithmic layer), presenting a ramp-like low-momentum zone when viewed from the side. As the hairpin packets grow they encounter other packets (Adrian, Balachandar & Liu 2001; Tomkins & Adrian 2003) leading to considerable scrambling of the vortices. For this reason it proves convenient in this study to use contours of low velocity to identify hairpin packets, as in Dennis & Nickels (2011), Lee & Sung (2011), Baltzer *et al.* (2013) and Lee (2017).

The 3-D visualization of typical very long low-speed structures in figure 1 uses a contour level of $u^+ = -2$. The streamwise extent of the figure is $10R$, and the azimuthal range is shown in the right corner. Three very long low-speed streaks that are slightly inclined to the spanwise direction are shown with lengths in excess of the entire field of view in the flow direction, and with characteristic widths of approximately $0.5R$ in the spanwise direction. These structures extend downwards to the near-wall region, consistent with the 'footprints' described by Hutchins & Marusic (2007*a*) for modulation of small-scale structures in the near-wall region. They also extend upwards through the outer layer and almost to the centreline of the pipe (see the colour contour).

Figures 2 and 3 present time-evolutions of the 3-D flow field in the perspective and top views to show how VLSM 1 in figure 1 is created (VLSM 1 in figure 1

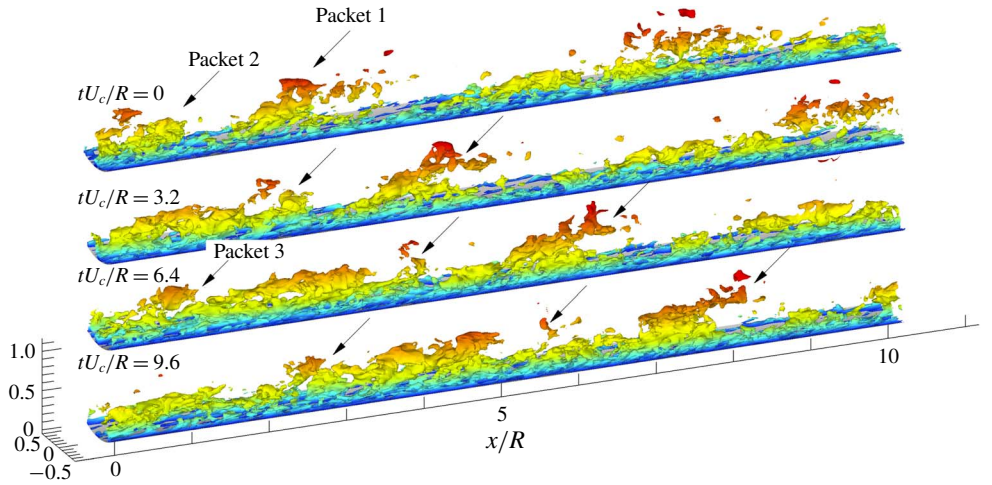

FIGURE 2. (Colour online) Perspective visualization of the time-evolving instantaneous low-momentum zones. The contour level is $u^+ = -2$, and the flow direction is from left to right. The colour legend is identical to that in figure 1.

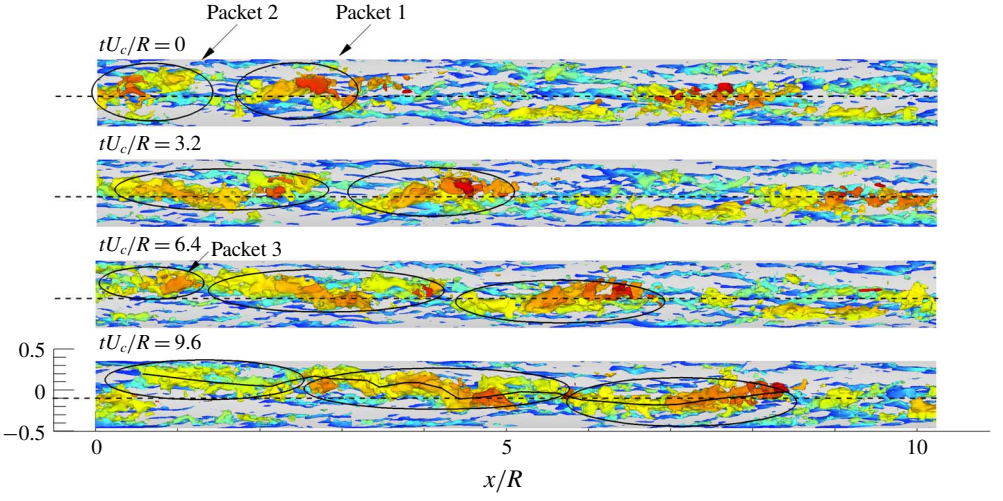

FIGURE 3. (Colour online) Top view of the time-evolving low-momentum zones. The contour level is $u^+ = -2$, and the flow direction is from left to right. The ellipses indicate the LSMs. The colour legend is identical to that in figure 1. The solid line at $tU_c/R = 9.6$ indicates approximate centre position of the LSMs at each streamwise location.

corresponds to $tU_c/R = 9.6$ in figures 2–4). The contour level is $u^+ = -2$, and the time interval is $tU_c/R = 3.2$. Figure 4, showing temporal variation of the low-momentum regions in the x–y plane, completes the visualization. The data were extracted along the fixed spanwise location (horizontal dashed line) in figure 3, and the contour is adjusted to $u^+ = -1.0$ for clarity. At the initial time $tU_c/R = 0$, there are two adjacent ramp-like structures in figures 3 and 4, packet 2 ($x/R < 1.2$) and packet 1 ($1.5 < x/R < 3.5$) having lengths of 2–3R. These packets are LSM structures. They are inclined

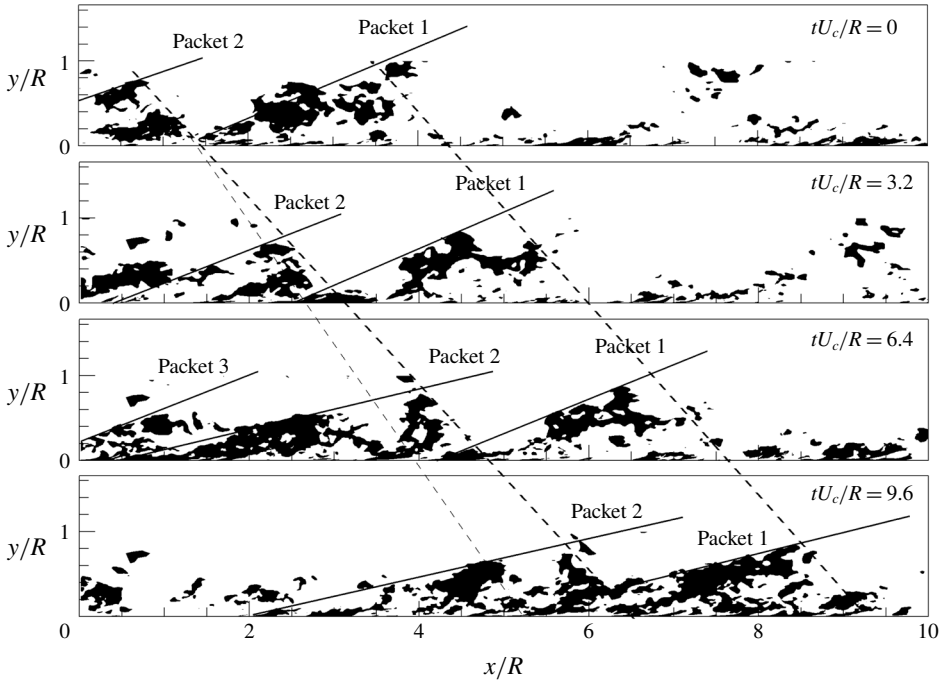

FIGURE 4. Evidence for the formation of VLSM through merging of LSMs. The black contours indicate the low-momentum regions ($u^+ = -1.0$). The data here are extracted along the streamwise-aligned dashed lines in figure 3. Solid lines indicate the approximate envelopes of the packets, and dashed lines are visible to show the streamwise trajectories of the travelling near-wall (thin) and outer layer (bold) structures.

at angles of approximately 15°–25° to the wall, and they are presumably the oldest and largest packets because they extend over a substantial region of the pipe core, typically up to $0.6R$. Smaller, younger packets can also be seen, and to distinguish them from the largest packets we shall refer to the smaller packets simply as packets. Note that the angle of the LSM packet ramps is larger than the 10°–15° mean angle of first generation packets (Christensen & Adrian 2001; Adrian 2007). The reason will be described later. LSM packets 1 and 2 evolve slowly in time, moving with almost equal convection velocities along the downstream direction (figures 2–4). Because the outermost regions of packets 1 and 2 (corresponding to the heads or arches of the tallest hairpins) experience higher mean flow velocity than the lower regions, they move downstream faster than the lower-lying regions of the packets, as can be seen in figure 4, wherein bold and thin dashed lines connect high and low parts of the ramp-like low-momentum zones of packets 1 and 2 at four times. Their slopes indicate approximate convection velocities, and they closely match with the mean velocities at $y/R = 0.02$ and 0.35. This process results in two kinematic phenomena: (*a*) within each LSM packet the taller hairpins move downstream faster than the shorter hairpins, resulting in elongation of each packet; and (*b*) the heads of the hairpins move faster than their lower parts (necks and legs), resulting in shearing motion. Since shear is a combination of rotation and plane strain with stretching at 45° to the mean flow, inclined hairpin vortices in the packets must be intensified by stretching and inclined

forward by the rotation. As time increases the stretching of LSM packets 1 and 2 is clear in figure 4.

The tallest part of packet 2 (that appears to be a detached structure) overruns the near-wall part of packet 1 (figure 4), which moves more slowly in the streamwise direction. Eventually, the head of the upstream LSM packet 2 merges with the tail of the downstream LSM packet 1, the connection first beginning close to the wall and later extending beyond the logarithmic layer (see figure 2). At $tU_c/R = 6.4$, the tallest part of packet 2 starts to settle down into the valley-like region between the adjacent ramp-like low-momentum patterns, and the continuous interaction of the structures results in the connection of the packets at $tU_c/R = 9.6$, creating the longer structure of the VLSM. Lee *et al.* (2014) showed that the convection velocity of the low-speed region is lower than the mean streamwise velocity, whereas the velocity in the high-speed region exceeds the mean streamwise velocity. In addition, they found that the convection velocity depends on the strength of the velocity fluctuations, i.e. it is increased with an increase of the strength in the velocity fluctuations. As a result, these differences of the convection velocity lead to the concatenation between in-line low-speed structures. In figure 4, the connecting structure residing in the valley seems to be trapped between the packet 1 and 2 for a long time, presumably because it cannot travel downstream due to packet 1. As a result, the VLSM maintains its coherence for a relatively long time.

After $tU_c/R = 9.6$, the adjacent packets 1 and 2 are completely merged at the downstream, and they form a long, but hardly straight, low-momentum zone travelling in the streamwise direction (figure 3). The pattern gives an appearance of meandering, but this is caused by the lateral offset of the merging packets, not by temporal spanwise oscillations. The merged low-momentum zone appears to make a smaller angle with respect to the wall (figure 4) owing to its length being approximately doubled without a concomitant increase in height.

In addition to the stretching, shearing and merging process, we have also found examples in the database where VLSM longer than $3R$ begins as a single structure (shorter than $3R$) and grows much longer without merging. However, this type of event occurs infrequently in our DNS dataset, and the merging event shown in figures 2–4 is the primary mechanism by which scales of motion larger than the LSMs formed. Statistical evidence indicating the commonplace occurrence of this mechanism will be provided later.

At $tU_c/R = 6.4$ in figures 2–4, another LSM packet-like structure (packet 3 designated by the arrow in figures 2 and 3) appears further upstream. Due to its spanwise-offset (see figure 3), packet 3 is not visible in figure 4 at $tU_c/R = 9.6$. Therefore, the upstream end of packet 2 observed at $tU_c/R = 0.0$ and 3.2 is probably a small portion of merged structure between LSM packets 2 and 3, and additional merging occurs with the downstream LSM packet 1. This is another indication of the commonplace nature of mergers leading to longer structures. Consistent with our observation, Lee *et al.* (2014) reported that in a turbulent channel flow the streamwise merging event between the LSMs is frequently observed near the wall, although the frequency of the merging event decreases far from the wall. The dominance of the merging event near the wall suggests that the energetic peak of the VLSMs in energy spectrum occurs near the wall compared to the LSMs (Monty *et al.* 2009).

The overall picture is consistent with the finding of Lee & Sung (2011), who studied the VLSM formation mechanism in the time-evolving fields of a boundary layer using DNS. Examination of the video of the spatially developing turbulent boundary layer on a flat plate made by Lee *et al.* (2012) also shows merging

between large packets in the manner just described. Furthermore, the signature of the velocity fluctuations by Kevin, Monty & Hutchins (2019) with a VLSM pattern is consistent with our observation, although they described the VLSM pattern using meandering. Thus, it has the potential to be a root cause of VLSM with a helical angle that is observed in significantly different outer flow geometry.

The streamwise concatenation process should not be confused with the near-wall auto-generation mechanism, which also creates longer sequences of hairpin eddies. Auto-generation is an organic growth process, whereas concatenation is mainly a simple piecing together (although interactions between the vortices of the merging LSMs may, and probably do occur).

The top view in figure 3 confirms that the very long structure at $tU_c/R = 9.6$ is not perfectly aligned along the streamwise direction, but inclined to the spanwise direction with negative azimuthal angle (see solid line). However, it should be noted that the primary body of LSM packet at $tU_c/R = 0.0$ and 3.2 tilts with positive spanwise-inclination angle. As LSM packet 1 merges with upstream LSM packet 2 at $tU_c/R = 6.4$ and 9.6, the upstream body of packet 1 alters its inclination from positive to negative (from downward to upward), and the two LSM packets concatenate with a very shallow angle. In this figure (at $tU_c/R = 9.6$), the inclined angle of the total VLSM is approximately 4°, in agreement with Baltzer *et al.* (2013). They suggested that as the packet-like entities concatenate in streamwise succession, there is also azimuthal offset of the LSMs with a dominant helical angle. In order to examine how the helical pattern of the VLSM is created in the present study, we considered the time-evolving instantaneous fields with larger field of view (not shown here). The result showed that packet 3 exists with a larger azimuthal offset than packet 2, and the continuous merging of packet 3 with the downstream packet creates a long low-momentum zone aligned along a helical path. The angle of the helical VLSM is determined by the pattern of the LSMs, i.e. the axial and azimuthal offsets prior to merger. The LSMs that are aligned without offset can form a VLSM having vanishing helical angle. The length of the VLSM also depends on the initial pattern of LSMs. For example, despite packet 1 stretching continuously, it does not encounter downstream packets that are old and large to be merger partners, and no additional mergers are observed out to $tU_c/R = 9.6$.

While the growth and alignment of spanwise-offset LSMs explains the formation of helical low-speed streaks on the VLSM scale, our understanding of the origin of VLSMs will not be complete until the genesis of the offset alignment is explained. Ultimately, the final explanation must rest on a dynamical model that embodies the interaction of the different scales and shows how they evolve to a statistical equilibrium that contains the observed patterns and alignments. Such a model is not within the scope of this paper. Instead, we will attempt to document the patterns in both the VLSM and the LSM, and show how they are related.

4. Statistical analysis

If the formation mechanism observed in the instantaneous fields is a common occurrence, it must leave an imprint on the two-point spatial correlation coefficient of the streamwise velocity fluctuations, R_{uu}, defined as

$$R_{uu}(r_x, r, r_\theta; r_{ref}) = \langle u(x, r_{ref}, \theta, t)u(x', r, \theta', t)\rangle/\sigma_u(r_{ref})\sigma_u(r), \tag{4.1}$$

where σ_u denotes the root mean square value of u. Since fully developed, axisymmetric pipe flow is homogeneous in the x- and θ-directions, R_{uu} depends only on the

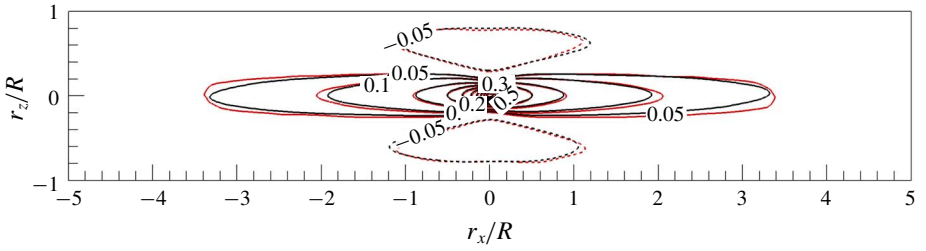

FIGURE 5. (Colour online) Contour lines of correlation coefficient R_{uu} in the r_x–r_z plane, with the reference point at $y_{ref}/R = 0.15$. Black lines are from the present DNS data, and dashed lines indicate negative values. Red lines from correlation contours found by Baltzer *et al.* (2013) are included for validation.

spatial separations $r_x = x' - x$ and $r_\theta = \theta' - \theta$. The brackets $\langle\cdot\rangle$ denote an average over time and x-θ. Figure 5 plots contours of R_{uu} in the r_x–r_z plane at $y_{ref}/R = 0.15$, where r_z is the separation in the z-direction denoted by $r_z = (R - y)r_\theta$. It shows an approximately $7R$ long region of positive correlation flanked by shorter regions of negative correlation on both sides in the spanwise direction. For the purpose of validation, isocorrelation contours for the present simulations are compared to the correlation found by Baltzer *et al.* (2013) at $Re_\tau = 685$. The agreement is reassuring, considering the differences in the DNS codes and Reynolds number.

Figure 6 shows 3-D views of R_{uu} and two-dimensional (2-D) contours in the cross-stream plane ($r_x = 0$) for various wall-normal reference locations. Above $y_{ref}/R = 0.3$, the highly elongated region of positive correlation is bracketed above and to the side by two long, anti-correlated regions, a space–time averaged manifestation of the high-momentum zones surrounding low-momentum zones in the instantaneous fields. The ramp-like contours of the positive correlations in the logarithmic layer are a common feature in turbulent boundary layers (Hutchins & Marusic 2007*a*; Lee & Sung 2011) and turbulent pipe flow (Baltzer *et al.* 2013), and we interpret them to be consequences of the low-momentum zones inside long hairpin packets.

Contours in the cross-sectional planes in figure 6(*a*,*b*) reveal weak, but significant, positive correlation between the reference location at 0° and locations centred at ∼140° and ∼220°. The proximities of these correlation maxima to 140° and 220°, suggest a three-wavelength Fourier mode in the θ-direction. This result is contrary to the hot-wire experiment of Bailey *et al.* (2008), who found no apparent correlation outside $|\theta| < 90°$ from the reference location. They concluded that long structures are not periodic in the azimuthal direction and that the interaction between the motions on the opposing sides of the pipe is minimal. Results from a POD of the present flow show long, energetic modes including 0, 1, 2, 3 and more wavelengths in θ. Summation of modes needed to construct the above correlation function could pull the location of the secondary positive maxima in figure 6(*a*,*b*) closer to 140° and 220°, perhaps explaining the slightly non-periodic spacing in θ. As the reference height is increased, the two red, anti-correlated regions gradually merge because the spanwise (or azimuthal) domain ($z = r\theta$) decreases with increasing wall-normal height, even as their spanwise length scale increases.

The two-point spatial correlation function averages the structural characteristics of eddies over all scales. Since our interest is in typical individual structures of the VLSM and LSM, we will divide u into two signals associated with the significantly different lengths of the VLSMs and LSMs and compute correlations of

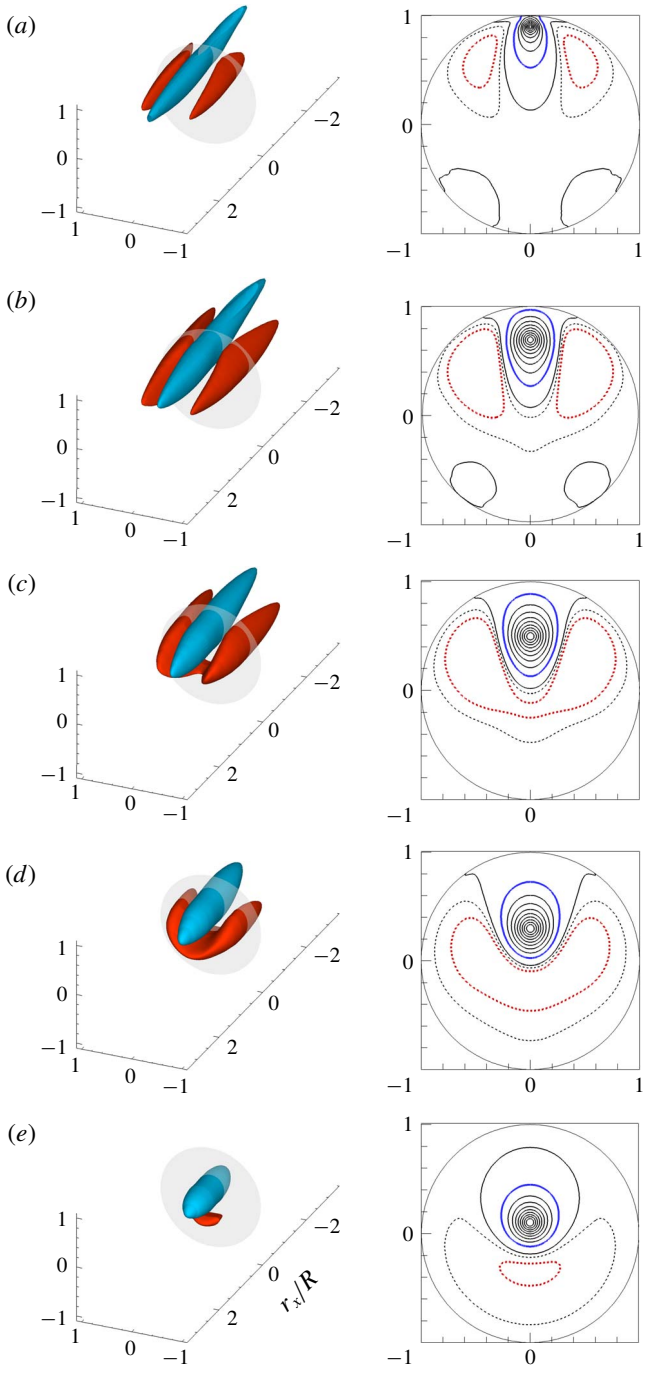

FIGURE 6. (Colour online) Correlation coefficient R_{uu} in 3-D perspective view. The 2-D slices on the transparent cross-stream plane at $r_x/R = 0$ are shown on the right-hand side. Reference points are located at (*a*) $y_{ref}/R = 0.1$, (*b*) $y_{ref}/R = 0.3$, (*c*) $y_{ref}/R = 0.5$, (*d*) $y_{ref}/R = 0.7$, (*e*) $y_{ref}/R = 0.9$. Isocontour levels for the 3-D view are $R_{uu} = 0.1$ (blue) and -0.05 (red), and contour spacing for the 2-D view is varied from 0 to 1.0 with an interval of 0.1 including -0.025 and -0.05. In the 2-D view, thick blue and red lines indicate $R_{uu} = 0.1$ and -0.05 corresponding to the isosurfaces in 3-D view.

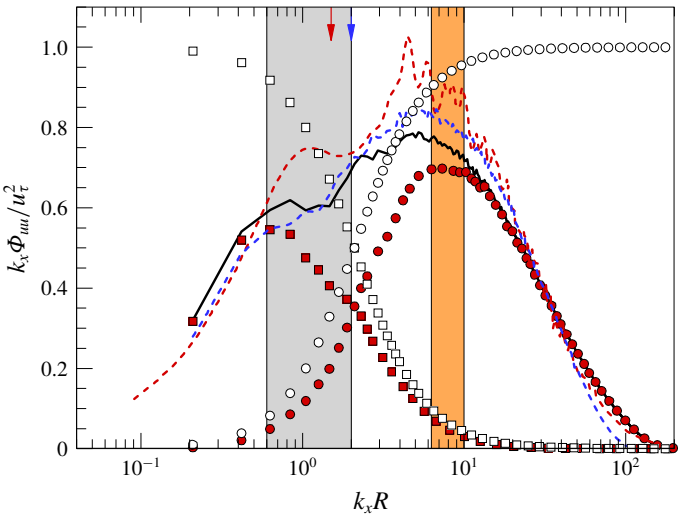

FIGURE 7. (Colour online) Pre-multiplied one-dimensional streamwise spectra $k_x\Phi_{uu}/u_\tau^2$. Solid line: present simulation data at $y_{ref}/R = 0.1$; red dashed line: experimental data from Kim & Adrian (1999) at $y_{ref}/R = 0.1$ and $Re_{D,cl} = 33\,800$ based on the pipe diameter and turbulent centreline velocity; blue dashed line: DNS data from Wu *et al.* (2012) at $y_{ref}/R = 0.1$ and $Re_\tau = 685$. The spectra for VLSM (square red symbols) and LSM (circular red symbols) are the result of decomposing the total spectrum using smooth low-pass (open squares) and high-pass (open circles) filters. The cutoff wavenumbers used to separate the VLSM from the LSM by Guala *et al.* (2006) at all y_{ref}/R and Bailey *et al.* (2008) at $y_{ref}/R = 0.2$ are shown with arrows for reference.

each to ascertain the spatial structures of the large and very large motions. Various approaches have been used to separate the motions, most using a sharp cut at a streamwise wavenumber demarcating the VLSM from the LSM. Figure 7 compares the pre-multiplied one-dimensional streamwise energy spectrum from our simulation with DNS data at the lower Reynolds number ($Re_\tau = 685$) at $y_{ref}/R = 0.1$ (Wu *et al.* 2012). Further, an experimental pipe spectrum measured by Kim & Adrian (1999) at $Re_\tau = 825$ is included, although this spectrum was not published in Kim & Adrian (1999). The experimental spectrum (red dashed line) clearly shows the bimodal shape characteristics in the logarithmic layer and there are two clear peaks in the experimental spectrum at $k_xR \sim 1$ and $k_xR \sim 4$, thought to indicate the VLSM and LSM, respectively. The long-wavelength peak (blue dashed line) for the DNS from Wu *et al.* (2012) appears attenuated relative to the experimental spectrum, but the present spectrum at the high Reynolds number (solid line) suggests that a long-wavelength peak occurs at long wavelength ($k_xR \sim 0.8$–0.9). Relative to the spectrum of our numerical simulation, the experimental peak at long wavelength is amplified despite of the low Reynolds number, an effect caused by the use of Taylor's hypothesis according to the theory of del Álamo & Jiménez (2006). Marusic & Monty (2019) reported that the long-wavelength peak is associated with the type-B eddies which are physically detached eddies that are expected to scale with the boundary layer thickness. The energy of the VLSMs or superstructures consist of the contribution from the type-A eddies (attached eddies) and type-B eddies, and there remains the question of how much energy comes from an individual eddy.

The wavenumber of the minimum between the two experimental peaks, at $k_xR \sim 1.5$, would be a well-defined candidate to divide the VLSM velocity from the LSM velocity, except that it fails to account for the lower energy of the VLSM spectrum relative to that of the LSM spectrum (Kim & Adrian 1999). As noted in the introduction, Guala *et al.* (2006) and Balakumar & Adrian (2007) used the slightly larger nominal value $k_xR = 2$ as the wavenumber separating the VLSMs and the LSMs because there is a clear change in the sign of the co-spectrum of u and v around this value, and it corresponds to a mean wavelength of πR that is close to the mean length of LSMs found by Kovasznay *et al.* (1970). Bailey *et al.* (2008) and Bailey & Smits (2010) employed wavenumbers across the range $0.6 \leqslant k_xR \leqslant 1.5$ (depending on y/R) to divide the VLSM from LSM. The grey-shaded range in figure 7 contains all of the foregoing estimates of the wavenumber separating LSMs and VLSMs.

We have assessed the sensitivity of the respective spatial correlations to the separating wavenumber value. The magnitudes of the correlations are affected by the separating wavenumber, but spatial features, such as the scale and shape of the correlation contours are largely unaffected, in agreement with Bailey & Smits (2010). Therefore, when using a sharp boundary to distinguish large from very large we have chosen the wavenumber $k_xR = 2$ to be consistent with the work of Guala *et al.* (2006) and Balakumar & Adrian (2007). Note that filtered velocities obtained using mutually exclusive filters, such as the sharp cutoff filters, must be statistically uncorrelated.

While a single, nominal wavenumber separating large- from very-large-scale motions is convenient for purposes of discussion and characterization, it is not physical, because the spectra of the VLSMs and the LSMs are certain to overlap. Moreover, taking the inverse Fourier transform of sharply cut spectra to get the correlation functions can produce unphysical ringing due to the discontinuity. Hence, separation by filtering in streamwise wavenumber space is better done with a pair of overlapping, smoothly decreasing low-pass and high-pass filters, having energy transfer characteristics such as the two curves which consist of open squares and circles in figure 7.

The two-sided co-spectrum of u with streamwise wavenumber k_x and azimuthal wavenumber k_θ is defined as

$$S_{uu}(k_x, r, k_\theta; r_{ref}) \equiv \frac{1}{(2\pi)^2} \int_{-\infty}^{\infty} \mathrm{e}^{-\sqrt{-1}(k_x r_x + k_\theta r_\theta)} R_{uu}(r_x, r, r_\theta; r_{ref}) \sigma_u(r_{ref}) \sigma_u(r)\, \mathrm{d}r_x\, \mathrm{d}r_\theta. \quad (4.2)$$

If u_{vl} is obtained by passing u through a low-pass filter $H_{vl}(k_x)$ its co-spectrum is

$$S_{vl}(k_x, r, k_\theta; r_{ref}) = |H_{vl}(k_x)|^2 S_{uu}(k_x, r, k_\theta; r_{ref}). \quad (4.3)$$

If $r = r_{ref}$, (4.3) becomes the power spectrum of u_{vl} on the plane at y_{ref} $(= 1 - r_{ref})$. The high-pass filter that defines the LSM plus smaller scales must satisfy

$$|H_l(k_x)^2 = 1 - H_{vl}(k_x)|^2 \quad (4.4)$$

to conserve energy. The corresponding dimensionless spatial correlations are

$$R_{vl}(r_x, r, r_\theta; r_{ref}) = \int_{-\infty}^{\infty} \mathrm{e}^{\sqrt{-1}(k_x r_x + k_\theta r_\theta)} |H_{vl}(k_x)|^2 S_{uu}(k_x, r, k_\theta; r_{ref})\, \mathrm{d}k_x\, \mathrm{d}k_\theta / \sigma_u(r_{ref}) \sigma_u(r), \quad (4.5)$$

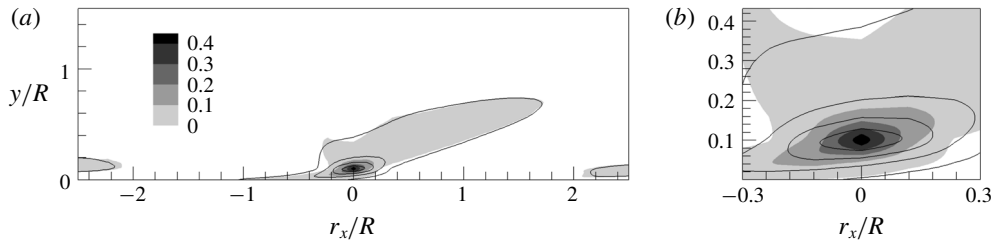

FIGURE 8. Correlation coefficient R_l for the LSMs at $y_{ref}/R = 0.1$ in the r_x–y plane. Grey shading indicate contours of the correlations of the LSMs plus small scales (i.e. $k_xR > 2$), and solid lines are the contours of correlation of LSMs only (i.e. $2 < k_xR \leqslant 10$). (*b*) Enlarged-view. Line contour levels are 0.005, 0.1, 0.2, 0.3 and 0.4.

$$R_l(r_x, r, r_\theta; r_{ref}) = \int_{-\infty}^{\infty} \mathrm{e}^{\sqrt{-1}(k_x r_x + k_\theta r_\theta)} |H_l(k_x)|^2 S_{uu}(k_x, r, k_\theta; r_{ref})\, \mathrm{d}k_x\, \mathrm{d}k_\theta / \sigma_u(r_{ref})\sigma_u(r). \tag{4.6}$$

Note that R_{vl} and R_l are not ordinary correlation coefficients because they have been normalized by the mean square value of u in order to describe the relative contributions of the VLSM and LSM to the total energy. Hence

$$R_{vl}(0, r_{ref}, 0; r_{ref}) = \sigma_{vl}^2/\sigma_u^2 \quad \text{and} \quad R_l(0, r_{ref}, 0; r_{ref}) = \sigma_l^2/\sigma_u^2, \tag{4.7a,b}$$

where

$$\sigma_{vl}^2 = \overline{u_{vl}^2(r_{ref})}, \quad \sigma_l^2 = \overline{u_l^2(r_{ref})} \quad \text{and} \quad \sigma_u^2 = \overline{u^2(r_{ref})}. \tag{4.8a–c}$$

The filters ($|H_{vl}|^2$ and $|H_l|^2$) shown in figure 7 were constructed to satisfy (4.4) and

$$|H_{vl}|^2 = (\tfrac{1}{2})^2 = |H_l|^2 \quad \text{at } k_xR = 2, \tag{4.9}$$

making the LSMs weaker than the VLSMs below $k_xR = 2$, and the VLSMs weaker than the LSMs above $k_xR = 2$. The red squares and circles in figure 7 represent the power spectra of u_{vl} and u_l, given by the products of the VLSM and LSM filter functions with the power spectrum of u. This decomposition presents a simple picture of two modes having peaks at $k_xR \sim 0.5$–0.8 and $k_xR \sim 8$ with a dividing boundary at $k_xR = 2$.

The foregoing decomposition does not attempt to separate the LSM from those in the inertial sub-range and the dissipation range. In their study of a high Reynolds number boundary layer, Hutchins & Marusic (2007*b*) separated the large scale from the small scales at $\lambda_x = R$ ($k_xR = 2\pi$), and in their POD analysis Bailey & Smits (2010) used $\lambda_x \sim 0.6R$ ($k_xR = 10$), while in their previous study (Bailey *et al.* 2008) the smaller scales were included in the LSMs. The various wavenumbers that have been used to define the LSM/small-scale boundary fall in the orange band in figure 7. Following Bailey & Smits (2010) we have chosen $k_xR = 10$ for the nominal boundary. Figure 8 compares correlation coefficients R_l computed by Fourier-transforming the power spectrum of u over $k_xR > 2$ (i.e. including the small scales), and $2 < k_xR \leqslant 10$ (excluding the small scales). The grey contours indicate the correlation R_l including the smaller scales, and the solid lines indicate the correlation excluding the small scales. The border between lightest grey and white is the 0.005-contour level to

highlight the LSMs. At large separations the small scales have little effect on the LSM correlation (figure 8*a*). The contour shape near the reference location is created by the induced velocity of strong second-quadrant ejection motions beneath the heads of hairpins. The weak correlation between the tallest packet of the LSM (far from the wall) and the LSM in the logarithmic layer ($y_{ref}/R = 0.1$) is consistent with the attached eddy model in which another type of eddies (termed type-B eddies) which are physically detached from the wall are important far above the logarithmic layer (Marusic & Monty 2019). The streamwise separation (approximately $\pm 2R$) of the positive correlation contours from the reference position indicates that the R_l structure is $\sim 2R$ long, and the correlation gives good picture of bulges. Contrary to the large-scale component, at separations less than $0.3R$ the small-scale components with wavenumber $k_x R > 10$ make substantial differences (figure 8*b*). Since our primary interest is the organization of the long wavelength components for the LSMs (low contour levels), it is not important to exclude the small-scale motions from the investigation of the LSMs.

In order to examine the spatial organization pattern of the VLSM and LSM, individual 2-D correlation contours of the VLSM (R_{vl}) and LSM (R_l) are estimated. This investigation is particularly important for a better understanding of the formation of the VLSM because the LSMs creating a VLSM by the concatenation process are also associated with the generation of the LSM patterns (R_l), as will be shown later. Figure 9 shows 2-D contours of the correlations of the VLSM (R_{vl}) and LSM (R_l) in the streamwise-radial plane. The contours of R_{vl} clearly indicate a structure that is asymmetric in the streamwise direction and tilted at a small angle $\sim 4°$ with respect to the wall. This behaviour is contra-indicative of long, streamwise homogeneous roll-cell structures, which would have no asymmetry and no tilt (Baltzer *et al.* 2013). Except at $y_{ref}/R = 0.1$, where the correlation is weighted to the downstream, the structures of the VLSM in the outer layer ($0.3 \leqslant y_{ref}/R \leqslant 0.9$) reside primarily upstream of the reference point. This effect and the foregoing tilt and asymmetry are consistent with the shape of the low-momentum zone within a single hairpin packet, except that the inclination of the centroid of the low-momentum zone of single packet correlations is expected to be larger. These observations, combined with the length of the correlation concept, are consistent with concatenated hairpin packets. Compared to the VLSM correlations, the LSM correlations (figure 9) in the outer layer contain elements in the lower level contours that indicate structural inclination at clearly larger angles. At $y_{ref}/R = 0.1$, the 15°–20° angle is consistent with established values for the envelope of hairpin packets in the logarithmic layer, but further up the angle steepens to approximately 45°, consistent with inclination angle of individual hairpins within packets. The streamwise extent of the LSM correlations shows little or no bias fore or aft, suggesting that the effect of differential convection due to mean shear is small.

The correlation functions of the streamwise velocity of VLSM and LSM are examined on the cross-stream plane in figure 10. The bold zero contours separate regions of positive and negative correlation. Positive correlations of the VLSM are flanked by regions of negative correlation, indicating long, low-momentum zones flanked by high momentum zones, or vice versa. The positive regions extend to the near-wall layer, even for reference heights up to $y_{ref}/R = 0.9$, showing clearly the influence of the footprints of the VLSMs on the near-wall region (Mathis *et al.* 2009). Two secondary regions of weak, positive VLSM correlation occur at $\sim 140°$ and $\sim 220°$ from the event location at 0° for reference points lying below $y_{ref}/R = 0.5$. They, too, penetrate the near-wall region. Baltzer *et al.* (2013) observed similar patterns of weak, positively correlated streaks in R_{uu} up to approximately $y_{ref}/R = 0.4$.

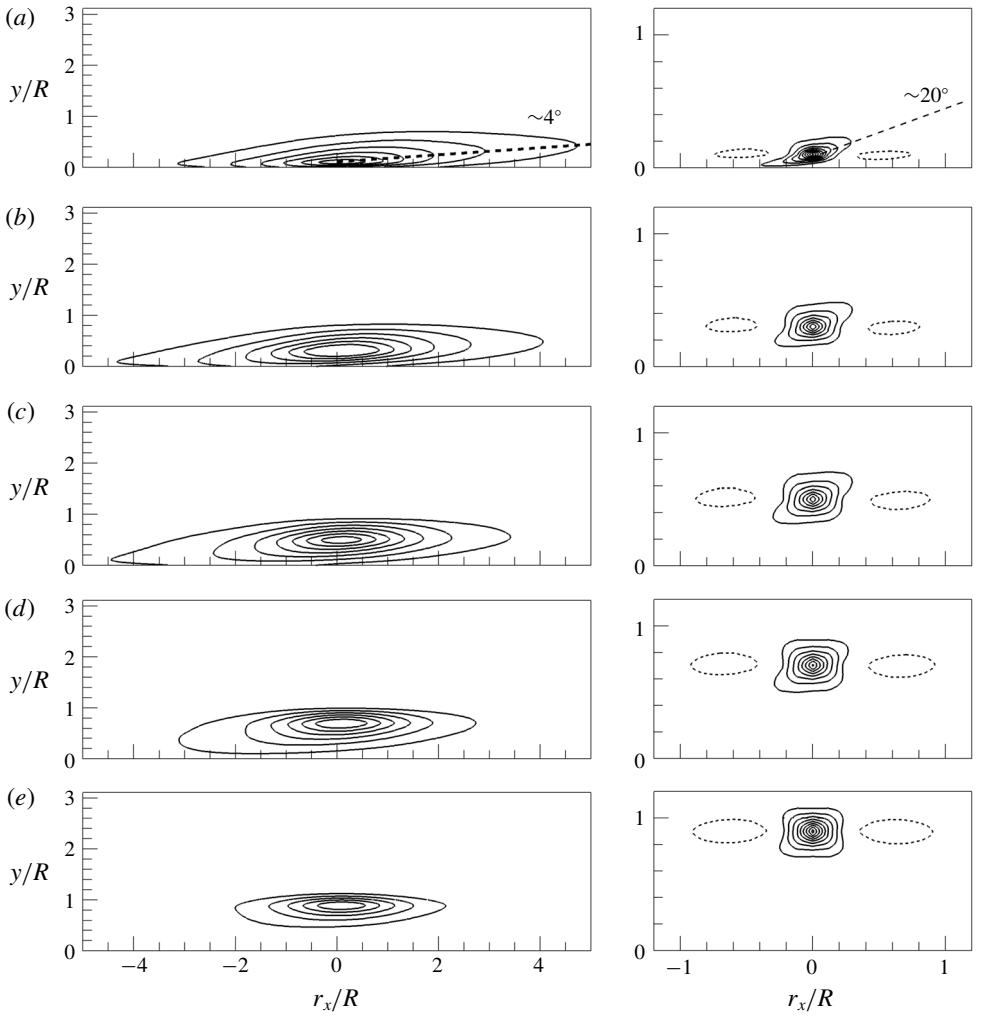

FIGURE 9. Correlation coefficient R_{vl} (lef-hand side) and R_l (right-hand side) in the r_x–y plane. (*a*) $y_{ref}/R = 0.1$, (*b*) $y_{ref}/R = 0.3$, (*c*) $y_{ref}/R = 0.5$, (*d*) $y_{ref}/R = 0.7$, (*e*) $y_{ref}/R = 0.9$. In R_{vl}, contour levels are varied from 0.05 to 0.3 with an interval of 0.05, and in R_l, contour levels are varied from 0.05 to 0.45 with interval of 0.05. A negative contour level of -0.05 is included in R_{vl} and R_l (dashed line). The mean inclination angles based on a contour level of $R = 0.05$ are shown.

The 0-contour R_l (right-hand side of figure 10) fails to convincingly reveal secondary regions of positive correlation, but the grey contour level on which $R_l = 0.0005$ does show secondary regions of positive correlation, especially at $y_{ref}/R = 0.3$ and 0.5. Unlike the secondary positive correlation regions of the VLSMs, those of the LSMs depend strongly on the wall-normal location of the reference points, separating from the wall with increasing y_{ref}/R and disappearing above $y_{ref}/R = 0.7$. The LSMs separate in the sense that the regions of positive correlation at $r_x/R = 0$ in R_l do not reach the wall at $y_{ref}/R \geqslant 0.1$. However, the 2-D contour of R_l in the r_x–y plane in the logarithmic layer (figure 8) is attached to the wall at an upstream location. The contribution of the attached hairpin vortex to the generation

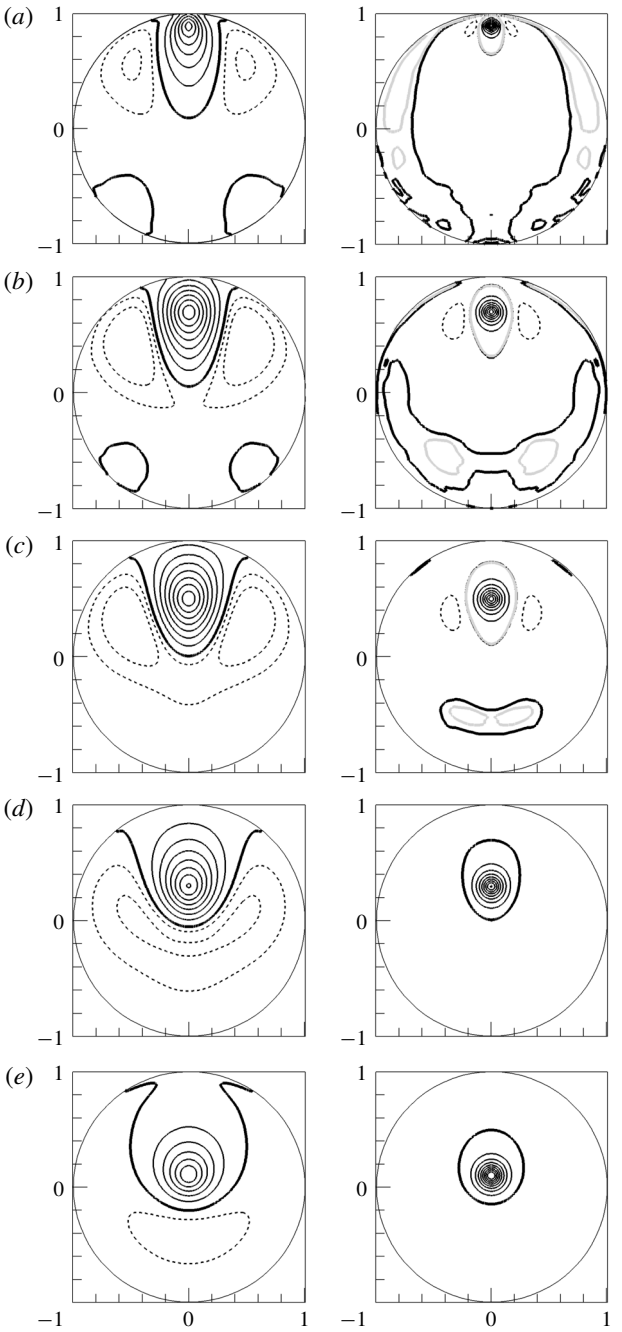

FIGURE 10. Correlation coefficient R_{vl} (left-hand side) and R_l (right-hand side) in the cross-stream plane. (*a*) $y_{ref}/R = 0.1$, (*b*) $y_{ref}/R = 0.3$, (*c*) $y_{ref}/R = 0.5$, (*d*) $y_{ref}/R = 0.7$, (*e*) $y_{ref}/R = 0.9$. Contour levels are varied from 0 to 0.4 with an interval of 0.05 including -0.025 and -0.05. The bold black solid line indicates the 0-contour level and dashed lines indicate negative values, respectively. For R_l in (*a–c*), the correlation contour of 0.0005 is depicted with a bold grey solid line.

of the correlation patterns in the logarithmic layer is consistent with Townsend's attached eddy hypothesis in which geometrically self-similar attached eddies occur in a hierarchy of scales with a population density of eddies that varies inversely with size and thus with distance from the wall (Townsend 1976; Marusic & Monty 2019). However, the less streamwise coherence of the correlation contours above the logarithmic layer (figure 9) implies that detached eddies, which may be formed locally away from the wall or are physically detached due to a saturation of the self-similar growth of hairpins attached to the wall, play a dominant role to generation of the correlation patterns.

Bailey & Smits (2010) reported that the azimuthal scales of the LSMs in the wake region (termed 'detached LSMs') and the VLSMs in the logarithmic layer are approximately the same, leading them to suggest that, and if the hypothesis of Kim & Adrian (1999) is valid, then only the larger, older, detached LSMs in the outer layer rather than the smaller hairpin packets located near the wall align to create VLSMs. In figure 10, we find the same approximate equality of azimuthal length scales of the VLSM in the logarithmic layer and the LSM in the outer layer ($y_{ref}/R > 0.5$), despite the wavenumber separating VLSM and LSM differing from that of Bailey & Smits (2010). Based on the observations of LSMs in the outermost edge of the boundary layer (Kovasznay *et al.* 1970; Falco 1977), Kim & Adrian (1999) and succeeding publications from that group have consistently defined LSMs in pipes and channels to be 2–3R long structures whose wall-normal extent approaches the centreline. They have further interpreted the LSMs to be the oldest and therefore largest packets. Since the largest packets contain smaller packets in a hierarchy of scales (Adrian *et al.* 2000), the attached smaller packets in the near-wall region with strong streamwise fluctuating velocity contribute to align the adjacent packets. Note that in figure 4, the tallest detached packet was shown to overrun the near-wall attached packet to form the VLSM. This scenario suggests that the LSMs and VLSMs are interrelated.

Figures 11 and 12 display correlation coefficients R_{vl} and R_l in the r_x–r_z plane using low values to expose the LSM and VLSM patterns (large correlation coefficients occur at small separation by virtue of the small-scale contributions; to see the large scales, one must accept the low correlation coefficients that occur at large separations). Correlation on the plane $y_{ref}/R = 0.15$ is included for future reference. The contour levels range from -0.05 to 0.1, with solid and dashed lines corresponding to contour levels of 0, 0.001 and -0.001. Below $y_{ref}/R = 0.5$ the contours of R_{vl} exhibit X-shaped patterns at very-large-scale separations between 5R and 10R (the regions in yellow). We will see that the X is a superposition of positively and negatively inclined alignments of LSMs along shallow ($\sim$5°–10°) helical angles. The helical angle of the VLSM and the LSM is defined as the mean of the largest and smallest helical angles, as shown in figures 11(a) and 12(a). At separations less than 5R the X-shape merges into a red region of high correlation flanked by spanwise-offset regions of negative (blue) then positive (pale yellow) correlation. In the streamwise direction the correlation briefly turns negative at approximately 8-9R, then resumes a positive value. As noted in Baltzer *et al.* (2013) the presence of the features at these low contour levels is due neither to noise, nor lack of statistical convergence, nor streamwise periodicity of the simulation, because previous experimental studies reported similar behaviour. The X-shape correlation pattern has also been reported in a boundary layer study using Taylor's hypothesis (Hutchins & Marusic 2007*a*). They also showed that an X-shape could be produced by correlating three adjacent, 12R-long strips of high–low–high speed flow that meandered sinusoidally in the spanwise direction. The single frequency meandering created periodic regions of

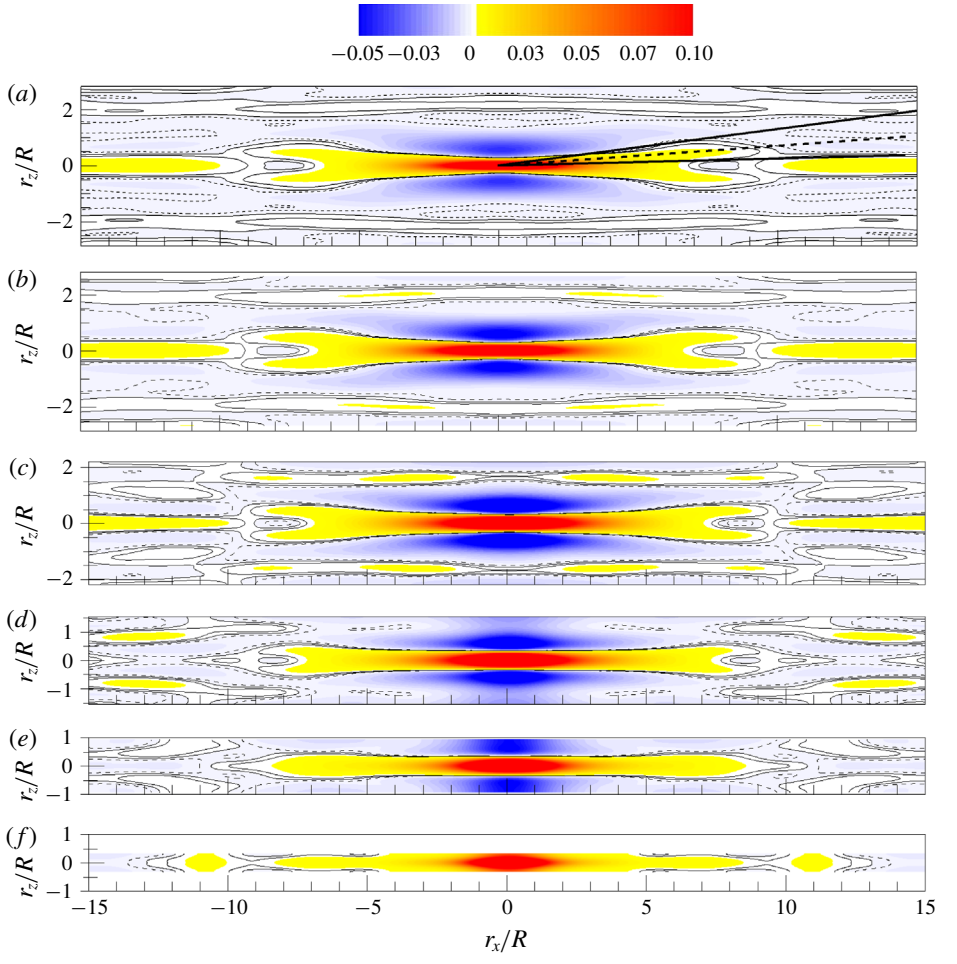

FIGURE 11. (Colour online) Correlation coefficient R_{vl} in the r_x–r_z plane. (*a*) $y_{ref}/R = 0.1$, (*b*) $y_{ref}/R = 0.15$, (*c*) $y_{ref}/R = 0.3$, (*d*) $y_{ref}/R = 0.5$, (*e*) $y_{ref}/R = 0.7$, (*f*) $y_{ref}/R = 0.9$. Colour contour levels are varied from −0.05 to 0.1, and solid lines depict the low contour levels of the correlations, corresponding to 0, 0.001 and −0.001 (dashed line). Thick, straight solid lines in (*a*) indicate the largest and smallest helical angles for the VLSM, and thick, straight dashed lines depict the mean helical angle.

positive and negative correlation in the streamwise direction with a period of $3.5R$. The similar positive region in our pipe flow simulation is more elongated ($r_x \sim 7R$) in figure 11 with additional regions of positive correlation offset in the streamwise and spanwise directions. However, it is hard to make such a pattern using a simple meandering low-speed streak. Later, we will show that the superposition of helically inclined VLSM modes, similar to those observed in the instantaneous fields, can induce complex spatial organization similar to that found in figure 11.

In figure 12, the correlation pattern of the LSM, R_l, also exhibits an X-pattern, but the angle of inclination is much larger than the helical angles found for the VLSM, and the streamwise and spanwise scales are, of course, smaller. The small region of positive correlation is surrounded fore-and-aft and side-to-side by regions of negative

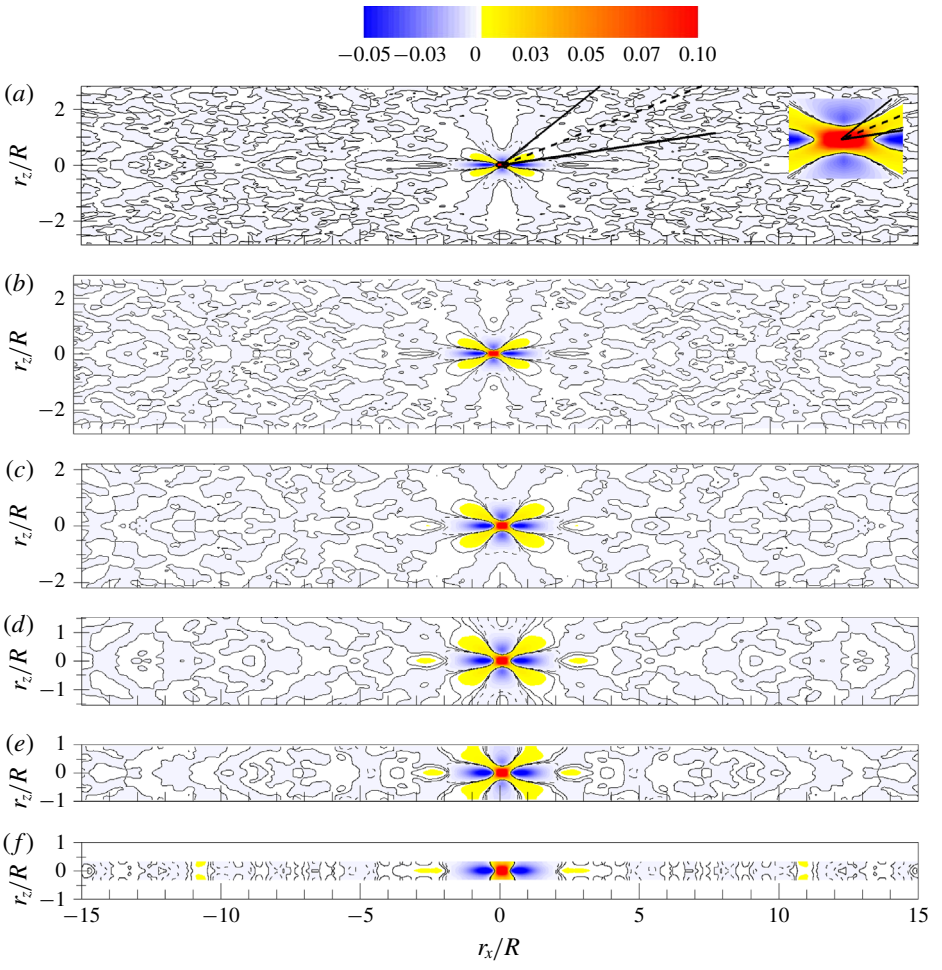

FIGURE 12. (Colour online) The same as figure 11, but for correlation coefficient R_l in the r_x–r_z plane. In (*a*), the enlarged view of a region in the vicinity of the reference location is included in the right-hand corner for clarity.

correlation. Although the region of positive correlation is surprisingly small, this pattern is consistent with the correlation of a single hairpin packet, but the X-pattern is not.

We now examine the variation of the correlation-based helical angles for the VLSM and the LSM along the wall-normal direction. Figures 11 and 12 make it clear that the helical angle depends on the value of the threshold employed. Since low contour levels of both VLSMs and LSMs create an X-shape pattern, we have chosen $R = 0.0005$ as a representative low contour level to measure the helical angles of the structures with opposite sign. In figure 13(*a*), the dominant helical angle of the VLSM (β_{vl}) is shown to decrease continuously with increasing y/R, probably due to the decrease of the azimuthal domain (figure 11), creating less helical angle. Contrary to the observation for the VLSMs, the highly tilted helical angle of the LSM (β_l) increases continuously in the outer layer (figure 13*b*). As shown in figure 12, the increase of the helical angle

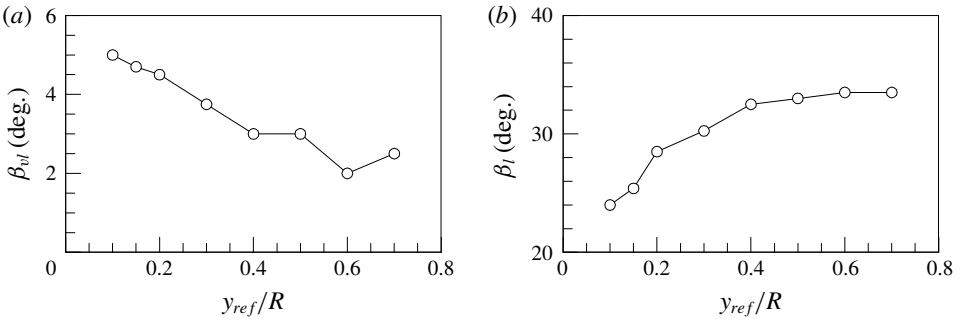

FIGURE 13. Azimuthally offset angle variations of the (*a*) VLSMs and (*b*) LSMs based on $R = 0.005$.

of the LSM seems to be due to high growth rate of the spanwise length scale of the LSMs than that of the streamwise length scale with the distance from the wall.

5. Reconstruction of R_{vl} and R_l

In this section, we will provide evidence that the spatial organization pattern of R_{vl} discussed in the previous section can be constructed by a combination of several helically aligned VLSM patterns based on energetic POD modes. The identified VLSM patterns that are created by artificial packets of hairpin vortices can reconstruct both R_{vl} and R_l based on spectral filtration of the signal.

5.1. *Proper orthogonal decomposition analysis*

We first consider the Karhunen–Loeve procedure to extract the most energetic coherent structures (POD modes) from the eigenfunctions of the two-point correlation tensor in the Fourier domain (Duggleby *et al.* 2007; Baltzer 2012)

$$\int_0^R S_{ij}(k_x, r, k_\theta; r_{ref})\hat{\Psi}_j^{(n)}(k_x, r, k_\theta) r\,\mathrm{d}r = \lambda^{(n)}(k_x, k_\theta)\hat{\Psi}_i^{(n)}(k_x, r_{ref}, k_\theta), \tag{5.1}$$

where $\hat{\Psi}$ is the Fourier-transformed eigenfunction with associated eigenvalue λ, and n is an index assigned to each POD mode by ordering according to decreasing energy. The spectral-density tensor S_{ij} is calculated from discrete Fourier-transformed velocity $\hat{u}_i(k_x, r, k_\theta)$ as

$$S_{ij}(k_x, r, k_\theta; r_{ref}) = \langle u_i(k_x, r_{ref}, k_\theta) u_j^*(k_x, r, k_\theta)\rangle, \tag{5.2}$$

where (*) denotes the complex conjugate of the eigenfunction. Due to the homogeneity and periodicity in x and θ each velocity component of the POD modes varies trigonometrically as a function of the x and θ spatial coordinates, i.e. the modes are Fourier in those directions. Each mode is assigned a mode number set (i_x, i_θ, n), where i_x and i_θ are indices for which the corresponding mode wavenumbers are

$$k_x = \frac{2\pi}{30R} i_x \quad \text{and} \quad k_\theta = i_\theta. \tag{5.3a,b}$$

In the latter, we will use both notions, (i_x, i_θ) and (k_x, k_θ), as convenient. Since the eigenvalue indicates the mean amounts of turbulent kinetic energy that each

	$i_x=0$	$i_x=1$	$i_x=2$	$i_x=3$	$i_x=4$	$i_x=5$	$i_x=6$
$i_\theta=0$	0.0164	0.0261	0.0212	0.0211	0.0136	0.0132	0.0116
$i_\theta=1$	0.1069	**0.1370**[1]	0.0744	0.0474	0.0534	0.0460	0.0428
$i_\theta=2$	**0.1464**[1]	**0.1616**	**0.1175**	0.0820	0.0649	0.0418	0.0421
$i_\theta=3$	**0.1416**[1]	**0.2038**	**0.1561**[1]	0.0969	0.0673	0.0383	0.0383
$i_\theta=4$	**0.2044**	**0.1487**	**0.1246**[1]	0.0686	0.0550	0.0399	0.0374
$i_\theta=5$	0.0912	0.0997	0.0882	0.0627	0.0473	0.0291	0.0235
$i_\theta=6$	0.0627	0.0512	0.0511	0.0495	0.0406	0.0274	0.0208

TABLE 1. Eigenvalue spectrum of the $n=1$ POD modes for the unfiltered pipe flow (e.g. using R_{uu} in the POD kernel). The eigenvalues in bold correspond to the 10 most energetic Fourier modes. The superscript 1 indicates mode combination 1.

POD mode contributes to reconstructed fields, the most energetic modes with $n=1$ are particularly important in organizing the flow. The $n=1$ eigenvalues for each streamwise and azimuthal wavenumber index in table 1 include the sum of all Fourier modes with positive and negative wavenumber values for the indices. The 10 most dominant modes are depicted in bold. The $n=1$ modes account for approximately 90 % of total kinetic energy for all (i_x, i_θ) pairs, and the most energetic modes are observed in VLSM wavelengths, consistent with a previous study of Baltzer *et al.* (2013).

The orthogonal eigenfunctions obtained from (5.1) can be used to reconstruct the two-point spatial correlation tensor with the corresponding eigenvalues. The two-point spatial correlation tensor is given by Baltzer (2012) and Holmes *et al.* (2012)

$$R_{ij}(r_x, r, r_\theta; r_{ref}) = \sum_{k_x}\sum_{k_\theta}\sum_{n} \lambda^{(n)}(k_x, k_\theta)\hat{\Psi}_i^{(n)}(k_x, r_{ref}, k_\theta)\hat{\Psi}_j^{(n)*}(k_x, r, k_\theta)\mathrm{e}^{j(k_x r_x + k_\theta r_\theta)}. \quad (5.4)$$

This equation (5.4) indicates that R_{ij} can be decomposed into the sum of the weighted (by λ) two-point correlation tensors of the eigenfunctions for all (i_x, i_θ, n) triples, and inverse Fourier transform back into physical space. Since the $n=1$ modes contribute most significantly to the flow, we focus on the structures of the $n=1$ mode. Furthermore, since the dominant X-shaped pattern in R_{vl} consists of wavelengths larger than $15R$ in figure 11, we shall focus on Fourier modes $i_x=0$, 1, 2; as an example, five energetic modes $(i_x, i_\theta, n) = (2, \pm3, 1)$, $(0, \pm2, 1)$, $(0, \pm3, 1)$, $(1, \pm1, 1)$ and $(2, \pm4, 1)$ with VLSM modes $i_x=0$, 1, 2. The modes are energy ordered in table 1, with $n=1$ being the most energetic mode. Their linear sum, properly weighted by $\lambda^{(n)}(k_x, k_\theta)$, is able to reproduce an X-shaped correlation pattern of R_{vl}, similar to that in figure 11(*b*) in the logarithmic layer. The components of the 4th, 6th, 7th, 8th and 9th energetic modes are grouped as mode combination 1 in table 1. These five modes are among the longest VLSM wavelengths more than $15R$ long, and the helical angles of the modes (β_{vl}) vary from 0° to 10.1° by the relation $\beta_{vl} = \tan^{-1}[(R-y)2\pi i_x/(L_x i_\theta)]$ at a particular y location with a wavenumber pair (i_x, i_θ) (Baltzer *et al.* 2013). The helical angle of $\beta_{vl} \sim 5.0°$ at $y_{ref}/R = 0.1$ indicates a mode relation $i_x \sim 0.464 i_\theta$, implying that the helical angle at this height is not simply obtained from a single dominant VLSM pattern, consistent with our previous observation in figures 10 and 11 with the secondary peak of the positive-offset regions closer to 140° and 220°. Although not shown here, another mode combination of eigenmodes can be made for R_{vl} with clear X-shape pattern, for instance using 4th, 7th, 8th and 9th energetic

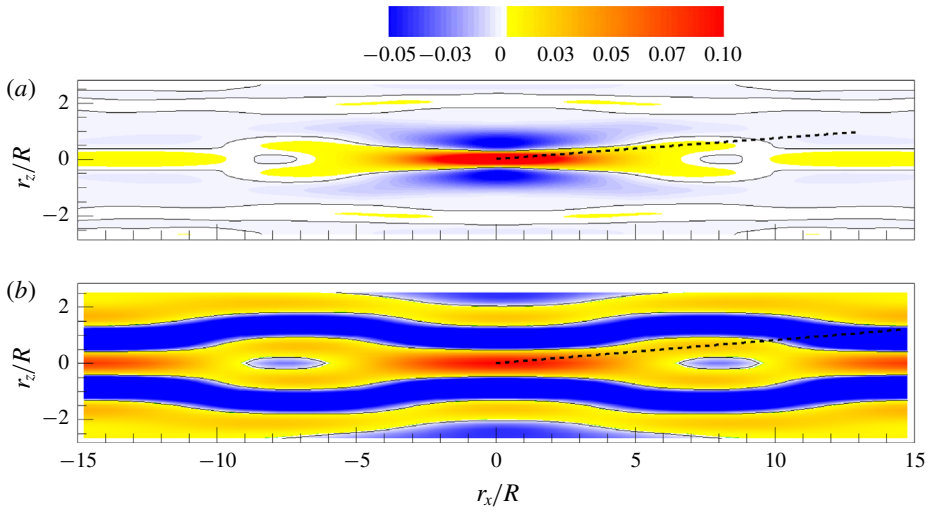

FIGURE 14. (Colour online) Correlation coefficient R_{vl} at $y_{ref}/R = 0.15$ in the r_x–r_z plane with (*a*) R_{vl} based on present DNS data and (*b*) R_{vl} based on superposition of the five energetic eigenmodes. Contour levels are varied from −0.05 to 0.1, and the solid lines depict the 0-contour level. Thick, straight dashed lines depict the mean helical angle ∼4.5°.

modes or 2nd, 4th, 7th, 8th, 12th, 14th, 16th and 18th energetic modes and so on. However, simply summing the five (or more) most energetic modes only provides a highly elongated correlation pattern in the streamwise direction without the X-shaped contour.

The streamwise-elongated pattern with no X-shape pattern and high energy is consistent with results by snapshot POD method that is based on no scale decomposition in x- and θ-directions to calculate POD modes (Hellström, Sinha & Smits 2011). In turbulent pipe flow at $Re_D = 12\,500$, they found that the most energetic POD mode ($n = 1$) that is the sum of all (i_x, i_θ) pairs consists of straight, streamwise-aligned segments of positive and negative streamwise velocity fluctuating structures. They also noted that the superposition of the four most energetic modes (n = 1–4) will recreate meandering structures, indicating that the alignment of spanwise-offset small scales of motions creates the appearance of VLSM.

Figure 14 shows correlation coefficients R_{vl} calculated from the present DNS data and from the superimposition of the above five energetic modes (mode combination 1) with positive and negative azimuthal wavenumber pair at $y_{ref}/R = 0.15$ (highest extent of logarithmic layer) in which VLSMs are frequently observed to be populated. The dominant X-shape pattern of the correlation with highly elongated positive region (∼7R long) shown in figure 14(*a*) is clearly apparent in the reconstructed R_{vl}. The mean helical angle of $\beta_{vl} \sim 4.5°$ (thick, bold dashed lines) averaged with the five energetic modes is in good agreement with the real one. In addition, positively correlated regions with the streamwise- and spanwise-offsets found in figures 10 and 11 are obviously shown with non-periodic spacing in x and θ, although the location of secondary positive maxima with the spanwise-offset in figure 14(*b*) is slightly closer to the reference location at $r_x/R = 0$. The difference of the contour levels between figures 14(*a*) and 14(*b*) is due to neglecting the other modes, and this indicates that other VLSM structures with different helical angles and wavelengths

are also important in constructing the full structural organization pattern of the true correlation R_{vl}. The similarity of the reconstructed R_{vl} to the real one demonstrates that the complex X-shaped correlation pattern of R_{vl} (or low contour level of R_{uu}) with the offset regions in the streamwise and spanwise directions is not simply due to a dominant outer layer large-scale structure (e.g. very long meandering motion). It also requires the superposition of helically inclined very long structures (4th, 8th and 9th modes) and streamwise-aligned motions (6th and 7th modes).

Figure 15 displays vector patterns of reconstructed v and w modes with isosurfaces of reconstructed u mode for the five dominant POD modes of mode combination 1. The vortices and associated large-scale patterns in the POD modes are periodically arranged along the pipe's circumference, and the modes take helical form encompassing all radii with rotation as x varies, unless i_x is non-zero. Here, we visualize counterclockwise modes. A similar set of clockwise modes also exists for oppositely signed azimuthal wavenumber. The most dominant patterns in figure 15 are those of roll-cells, indicating a close association with VLSMs. The strength of the roll-cell modes is maximum for $(i_x, i_\theta) = (2, 4)$, indicating that the strength of the roll-cells is proportional to the number of azimuthal wavenumber. In addition, the roll-cells clearly influence near-wall structures regardless of the POD mode pair, based on observations that the roll-cells are centred far from the wall at $y/R = 0.29$–0.41, and the roll-cells' influences are strong in the near-wall region, consistent with the interaction between inner and outer layers (Mathis *et al.* 2009). Although not shown here, linear estimates of conditional averages with a $-u$ event at $y_{ref}/R = 0.15$ using the VLSM correlation on the cross-stream plane exhibit large-scale counter-rotating roll-cells with strong eruptions and sweep motions, consistent with the reconstructed POD modes in figure 15 (blue colour). This indicates that the large roll-cells could sweep near-wall hairpin packets into alignment along the stagnation zones between cells (Toh & Itano 2005; Adrian 2007). However, it is not clear whether the roll-cell also nudges the LSMs into alignment, or the LSM alignment creates the roll-cells.

5.2. *Hairpin packet model*

To provide clear evidence for how spatial organization patterns of both R_{vl} and R_l are created in the flow field based on the model of VLSMs, we consider a hairpin model devised from the work of Perry & Chong (1982) and Perry & Marusic (1995). In their model, a hairpin has the shape of a goalpost inclined at 45° to the wall in the downstream direction. The induced velocity created by the model is calculated based on the Biot–Savart law.

Figure 16(a) shows the typical structure of a hairpin vortex represented by an isosurface of negative streamwise velocity. Here, the contour level is chosen to clearly show the hairpin-like structure with 20 % of minimum (negative maximum). The legs (or neck) of the goalpost-like hairpin are attached to the wall, and the inclination angle of the structure is maintained to be constant with 45° for simplicity. The packet in figure 16(b) consists of six hairpin vortices that are streamwise-aligned with spacing $0.5R$. The height (h) of the hairpins varies linearly from $0.1R$ to $0.7R$ with an interval of $0.12R$, creating a packet growing upwards in the streamwise direction at a mean angle of approximately $\alpha = 13.5°$ (Zhou *et al.* 1999; Adrian *et al.* 2000). Note that the width of the hairpins is taken to be twice that of the hairpin height based on the data of Tomkins & Adrian (2003). The induced velocity within and around a packet is simply the linear summation of the velocities induced by individual hairpin vortex. The induced velocity and correlation patterns by a

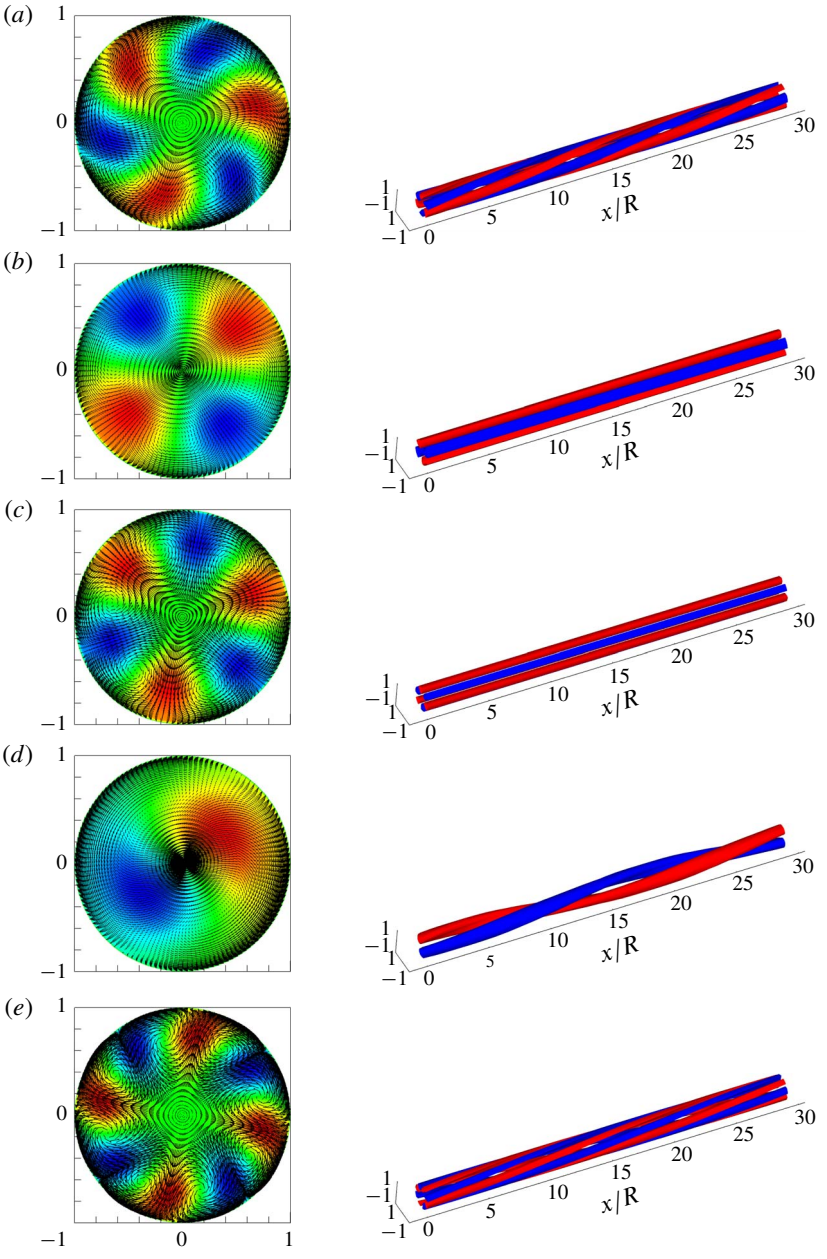

FIGURE 15. (Colour online) Roll-cell-like behaviour of the five POD modes with (*a*) ($i_x = 2$, $i_\theta = 3$), (*b*) ($i_x = 0$, $i_\theta = 2$), (*c*) ($i_x = 0$, $i_\theta = 3$), (*d*) ($i_x = 1$, $i_\theta = 1$) and (*e*) ($i_x = 2$, $i_\theta = 4$). The left-hand side plots display the colour contours of reconstructed u with in-plane velocity vectors of v and w modes at $x/R = 0$ planes, and the right-hand side red and blue isosurfaces indicate the swirling patterns of positive and negative u-structures (at one-half of maximum and minimum).

packet in figure 16(*c*,*d*) are similar to those found in the literature (Zhou *et al.* 1999; Tomkins & Adrian 2003).

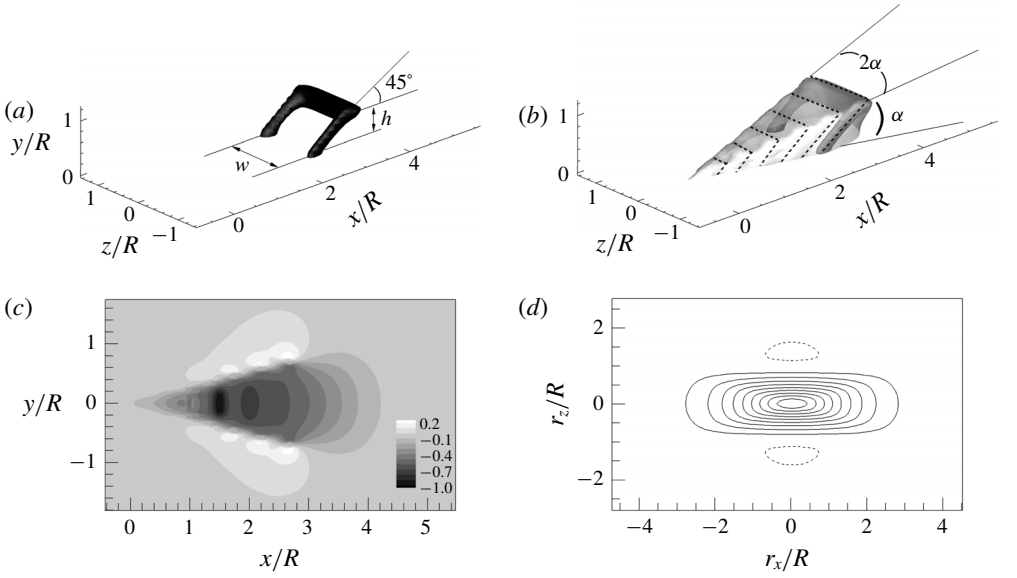

FIGURE 16. (*a*) Goalpost-like model of a single hairpin vortex (Perry & Marusic 1995). The hairpin is inclined to the flow direction with 45°. (*b*) Hairpin packet model (grey colour) constructed here using 6 hairpins (dashed lines). The height (h) of the hairpins is varied linearly from $0.1R$ to $0.7R$ and the width (w) is $2h$. The growth angle is constant, $\alpha = 13.5°$. The individual hairpins in (*b*) are separated with spacing of $\delta x/R = 0.5$ in the streamwise direction, creating a $3R$-long hairpin packet, enveloping an LSM. The hairpin in (*a*) is the 6th hairpin in the packet, as shown in (*b*) with transparent view. The isosurface contours in (*a*) and (*b*) are the negative streamwise velocity. (*c*) The u velocity induced inside and outside the model packet at $y_{ref}/R = 0.15$ (normalized by the negative maximum) and (*d*) line contours of the correlation coefficient of the streamwise velocity on the r_x–r_z plane at $y_{ref}/R = 0.15$. The contour levels are varied from 0.1 to 0.9, and the dashed line depicts $R = -0.05$.

We construct the five energetic VLSM modes described in § 5.1 by aligning the above artificially generated hairpin packets along helical angles (with spanwise-offset) that are very consistent with those of the five modes in figure 15. An example of an artificially constructed VLSM pattern corresponding to the counterclockwise 4th mode $(i_x, i_z) = (2, 3)$ is shown in figure 17(*a*) with its correlation patterns (*b*) R_{uu}, (*c*) R_{vl} and (*d*) R_l using the high- and the low-pass filters employed in figure 7. Here, the computational domain is $(L_x, L_y, L_z) = (30R, 1.25R, 2\pi * 0.85R)$ to be consistent with the domain size in the logarithmic layer in figures 14 and 15. The configuration in figure 17 is clearly shown when the cylinder in figure 15(*a*) is rolled out to be viewed as a plane at $y/R = 0.15$. In addition, figure 18 shows correlation patterns using both positive and negative spanwise wavenumber pair for the 4th mode, i.e. clockwise and counter-clockwise helices, compared to that in figure 17. Since the hairpin packets are continuously aligned along the helical alignment related to the 4th POD mode both with spanwise-offset and with a streamwise-interval similar to that between the hairpins, there exist 10 hairpin packets along the helical lines over the $30R$ long domain. As expected, the correlation R_{vl} with low contour level of R_{uu} in figure 17 shows that the highly elongated positive VLSM pattern is flanked by negatively correlated regions on each side due to vortex induction from the legs and

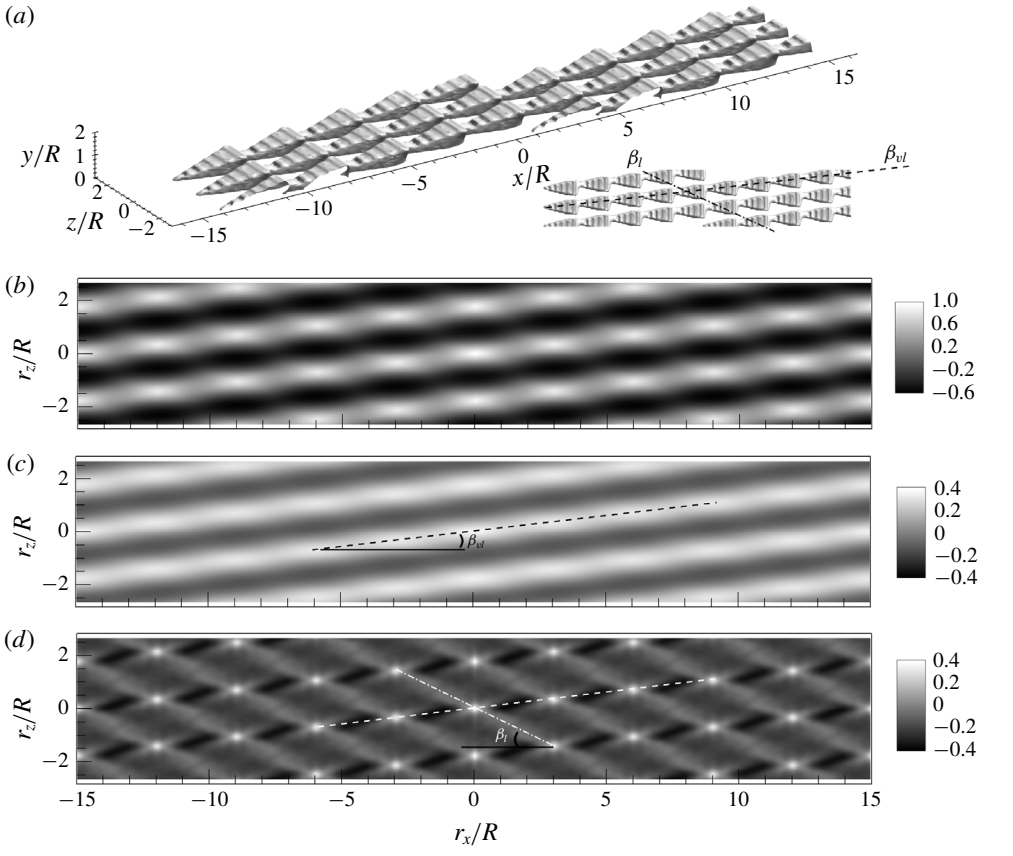

FIGURE 17. (*a*) Perspective view of the synthetically constructed pattern (u velocity with 20 % of minimum) associated with the counterclockwise 4th mode $(i_x, i_z) = (2, 3)$. The top view of the pattern is shown in the right-hand corner, and the flow direction is from left to right. Spatial two-point correlations using the pattern in (*a*) where (*b*) R_{uu}, (*c*) R_{vl} and (*d*) R_l. The high- and low-pass filters in figure 7 were employed, and the reference wall-normal height is $y_{ref}/R = 0.15$. The dominant helical angles for VLSM (β_{vl}) and LSM (β_l) are defined in (*c*) and (*d*) with dashed and dashed-dot lines. Here β_{vl} and β_l are $\sim$6.8° and $\sim$25.4° for the 4th mode. In addition, the relevant LSM patterns for β_{vl} and β_l are described in (*a*) with dashed and dashed-dot lines.

the head, and the correlation is inclined at a helical angle due to spanwise-inclined VLSMs related to the 4th mode. In addition, the correlations of R_{uu} and R_{vl} seem to contain meandering behaviour along the helically inclined VLSM alignment (see the top view in figure 17*a*), and it is more pronounced in R_{uu} rather than R_{vl} due to the smoothing effect of the VLSM filter. This demonstrates that the meandering is possibly due to spanwise-offset LSMs that are relatively straight, not due to a dominant meandering motion residing in turbulent flow. The meandering behaviour based on our result is consistent with the previous observations of Balakumar & Adrian (2007) that 'the smoothed field of a concatenation of misaligned hairpin packets would look like a pair of meandering counter-rotating streamwise vortices'. Furthermore, our result is consistent with the study of Hellström *et al.* (2011) based on snapshot POD modes in which they showed that reconstructions with the 10

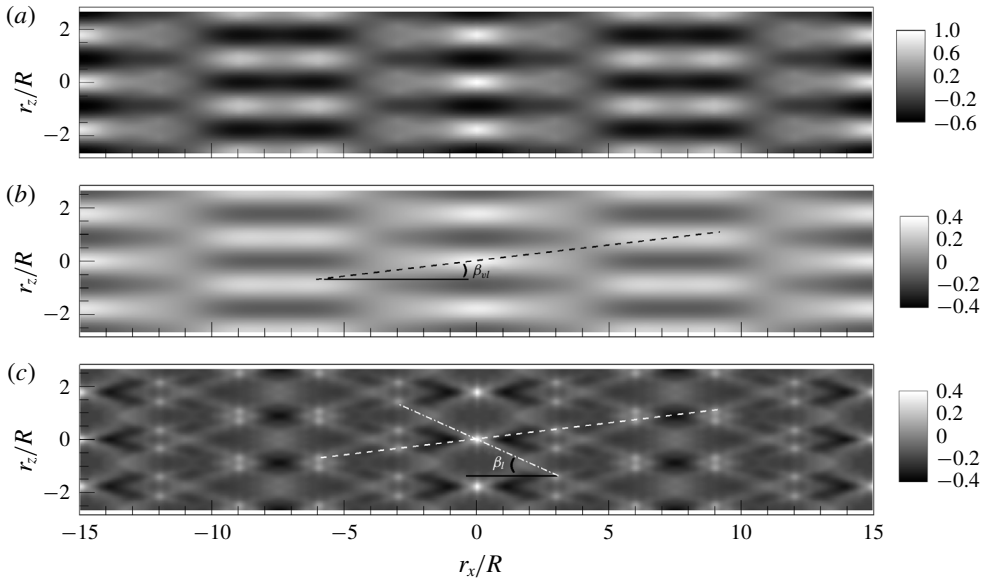

FIGURE 18. Spatial two-point correlations (*a*) R_{uu}, (*b*) R_{vl} and (*c*) R_l at $y_{ref}/R = 0.15$ using the artificial pattern in figure 17, but using both positive and negative spanwise wavenumber pair. The dominant helical angles for VLSM (β_{vl}) and LSM (β_l) present in figure 17 are shown in the figure.

most energetic POD modes ($n = 1$–10) capture all the principal characteristics of the VLSM, suggesting that VLSMs are constructed of the most energetic POD modes that give the impression of long meandering structures.

However, the correlation pattern of R_l in figure 17(*d*) shows a clear alternating pattern of positive (white) and negative (black) correlation regions at an angle of β_{vl} in the streamwise direction. This is attributed to high-momentum regions residing in the upstream of the low-momentum regions due to continuous induction of hairpin vortices, consistent with figure 12. Instead of the long coherent pattern along the angle of β_{vl} in R_l, an elongated pattern of positive correlation region is obviously shown to be created with an inclination angle (β_l), as depicted by a white dashed-dot line in figure 17(*d*). Since we assume that the most upstream packets in each line (along β_{vl}) are located in the region of $0 \leqslant x/R \leqslant L_l$, then the mode helical angle for the LSM at a particular y location and with a wavenumber pair (i_x, i_z) can be defined by

$$\beta_l = \tan^{-1}\left(\frac{(R-y)2\pi}{i_z}\left(\frac{1}{L_l} - \frac{i_z}{L_x}\right)\right), \tag{5.5}$$

where L_l is the streamwise length ($= 3R$) of each packet. Then, the (i_x, i_z) = (2, 3) mode has LSM helical angle of $\beta_l = 25.4°$ at $y/R = 0.15$ in figure 17(*d*). As can be seen in figure 17(*a*) with the dashed-dot line, such a positive correlation pattern of R_l along with the helical angle β_l is induced by the alignment of LSMs, although each LSM is involved in creating different VLSMs. Inspection of the other four modes with their configurations using the above relation in figure 19 shows helical angles of $\beta_l = 41.7°$ ($i_x = 0$, $i_z = 2$), $30.7°$ ($i_x = 0$, $i_z = 3$), $57.9°$ ($i_x = 1$, $i_z = 1$) and $19.9°$ ($i_x = 2$, $i_z = 4$) with a similar organization pattern to the (i_x, i_z) = (2, 3) mode, although corresponding correlation patterns (i.e. R_{uu}, R_{vl} and R_l) are not shown here.

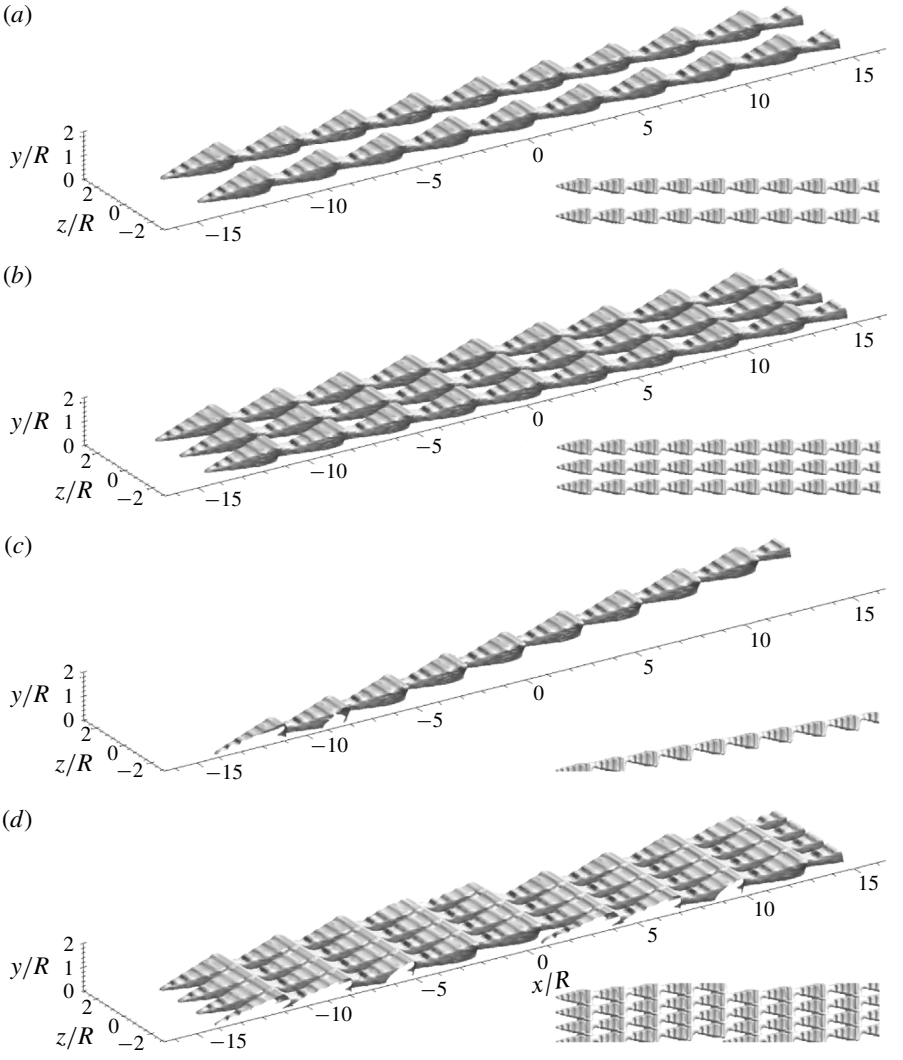

FIGURE 19. The same as figure 17(*a*), but for the other four modes. (*a*) 6th mode $(i_x, i_\theta) = (0, 2)$, (*b*) 7th mode $(i_x, i_\theta) = (0, 3)$, (*c*) 8th mode $(i_x, i_\theta) = (1, 1)$ and (*d*) 9th mode $(i_x, i_\theta) = (2, 4)$.

Although the VLSM mode of $(i_x, i_z) = (2, 3)$ is one of the most energetic modes in the eigenvalue spectrum and has wide influence in organizing the flow pattern, strong local energy contributions to the total energy are primarily from the sum of LSM and smaller scales of motions, as shown in figure 17(*d*) with deep white and black contours. The contour coefficients R_{vl} and R_l normalized by the mean square value of u in figures 10–12 also show the consistent behaviour to the energy contributions from LSMs and VLSMs. Baltzer *et al.* (2013) analysed an instantaneous field with an energetic mode $(i_x, i_z) = (2, 3)$, and they showed that the typical strength of the very long u-structure with the mode is more than 20 times smaller than that of the raw data at $y/R = 0.15$, indicating that the highly energetic VLSMs should be combined with smaller scales of motions contributing to strong local net energy to consist of a

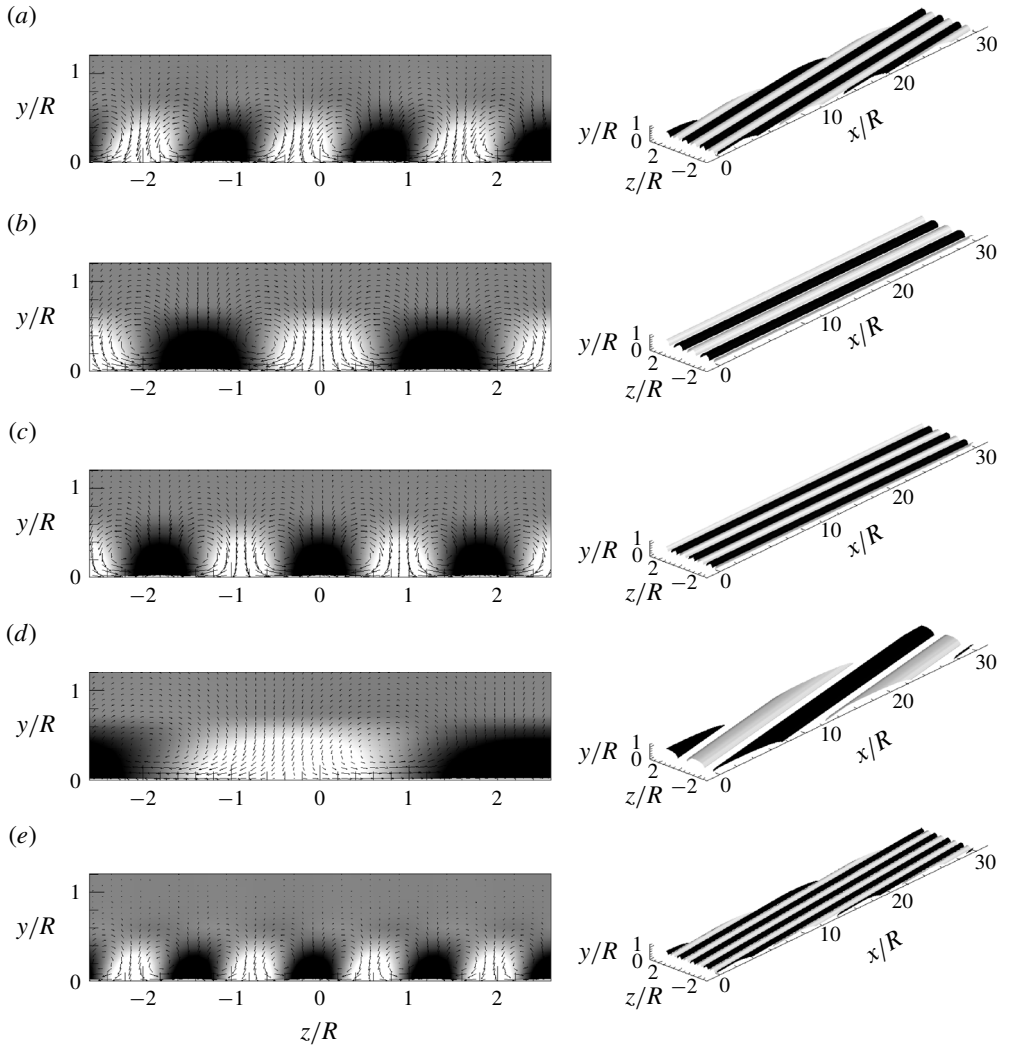

FIGURE 20. Roll-cell-like behaviour of the artificial five POD modes. Each POD mode is constructed using each artificially constructed VLSM pattern of the five energetic modes with positive and negative spanwise wavenumber pair. (*a*) $(i_x, i_\theta) = (2, \pm 3)$, (*b*) $(0, \pm 2)$, (*c*) $(0, \pm 3)$, (*d*) $(1, \pm 1)$ and (*e*) $(2, \pm 4)$. The left-hand plots display the colour contours of u with in-plane velocity vectors of v and w modes at $x/R = 0$ planes, and the right-hand white and black isosurfaces indicate the swirling patterns of positive and negative u-structures (at one-half of maximum and minimum).

total energy for a raw instantaneous realization. The energy relationship is consistent with the hypothesis that the largest scales are composed of concatenations of LSMs.

Figure 20 shows constructed POD modes using the artificially constructed VLSM patterns of the energetic five modes of mode combination 1. Here, each POD mode is calculated using each corresponding VLSM pattern with a positive and negative spanwise wavenumber pair among the five energetic modes, i.e. in figure 20(*a*), the artificial VLSM pattern, which resembles the pattern corresponding to the 4th mode $(i_x, i_z) = (2, \pm 3)$, is first made by the alignment of the artificial LSMs with

positive and negative spanwise wavenumber pair, and the energetic POD mode with wavenumber pair $(i_x, i_z) = (2, \pm 3)$ is constructed based on its correlation pattern shown in figure 18(*a*). This approach results in the most energetic $n = 1$ POD mode at the $(i_x, i_z) = (2, 3)$ wavenumber pair in figure 20(*a*), corresponding to the wavenumber pair related to the 4th energetic mode (figure 15*a*).

In figure 20, the very-large-scale counter-rotating roll-cell-like vortex patterns are periodically organized in the streamwise and spanwise directions except for the rotation when varying the streamwise location for non-zero i_x. The roll-cells for the modes are centred at $y/R = 0.28$, 0.34, 0.3, 0.37 and 0.2, and the trend of the position is comparable to $y/R = 0.33$, 0.38, 0.34, 0.41 and 0.29 in figure 15 for the real ones, although there are small discrepancies in magnitude. The roll-cell motions are present for either the streamwise-aligned or spanwise-inclined VLSM pattern, and the general shape of the contours for all the roll-cells is relatively insensitive to the number of roll-cell pairs, consistent with those in figure 15. This indicates that the artificial packet alignments for the VLSMs replicate the topology of the modal flow pattern for each five mode. However, some differences are clearly observed in particular in the near-wall region. That is, the isosurfaces of the roll-cells in the 3-D view in figure 20 are not closed in the near-wall region. The difference indicates that the model for the VLSM related to the roll-cells is not complete, and this could be attributed to the absence of consideration not only for interaction between inner and outer layers (Mathis *et al.* 2009) but also for a hierarchy of scales across most of the wall layer in this model (Adrian *et al.* 2000).

Significant efforts have paid attention to studying the roll-cell-like motions in previous studies based on a stability analysis calculation, conditional averaging conditioned by a u event, instantaneous analysis and POD modes (Toh & Itano 2005; del Álamo & Jiménez 2006; Hutchins & Marusic 2007*b*; Chung & McKeon 2010; Wu *et al.* 2012; Baltzer *et al.* 2013). However, it is not still clear for the origin of the roll-cells (i) that they could be generated by the collective behaviour of near-wall structures (Toh & Itano 2005), or (ii) that they could be amplified by the forcing of smaller modes (McKeon & Sharma 2010), or (iii) that they could be attributed to jittering of small-scale (Balakumar & Adrian 2007; Marusic & Hutchins 2008), or (iv) that they could be due to a linear instability mechanism (del Álamo & Jiménez 2006).

The existence of the roll-cells similar to the real ones in figure 20 demonstrates that roll-cells could be created by the VLSMs that are collectively formed by the concatenation of LSMs aligned in a straight manner or in a spanwise-inclined manner. As similar to the behaviour of the roll-cell in the near-wall region in figure 15, relatively strong influence of the roll-cells on the near-wall structures in figure 20 indicates that the large-scale roll-cells centred in the outer layer organize the entire flow with strong near-wall interaction, for example, near-wall small-scale modulation by outer layer VLSM (Mathis *et al.* 2009). Since the roll-cell created by the outer layer energetic VLSM (that are created by collective behaviour of smaller-scales) sweeps smaller-scale motions into beneath the VLSM pattern as shown in the vector fields in figures 15 and 20, the alignment of the small-scale motions along the line of the roll-cell by a sweep event can induce a footprint of the VLSM in the near-wall region. Furthermore, since the small-scale motions with sufficient strength can ultimately grow into LSM packets via auto-generation, the presence of the roll-cell mode can also induce the alignment of the LSM packets in a helical angle to form a VLSM, finally intensifying the roll-cell. A DNS study of a turbulent channel flow by Hwang, Lee & Sung (2016) provided evidence that

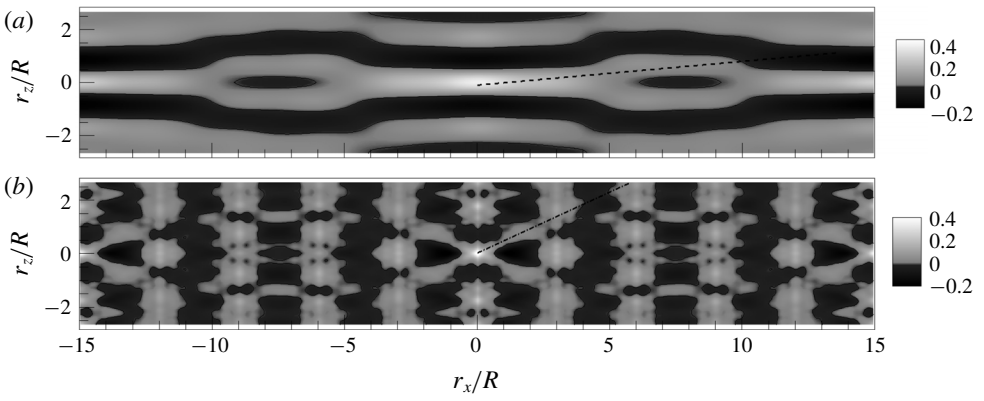

FIGURE 21. Superimposed correlation patterns in the r_x–r_z plane using the five artificial VLSM patterns with positive and negative spanwise wavenumber pair at $y_{ref}/R = 0.15$. Here (*a*) R_{vl} and (*b*) R_l. The mean helical angles of β_{vl} and β_l for VLSMs and LSMs are depicted by dashed and dashed-dot lines in (*a*) and (*b*).

the congregation of the near-wall streaks beneath the outer counter-rotating roll-cells generates intense velocity perturbations which are lifted away from the wall, resulting in the concatenation of LSMs to form a VLSM. This two-way interactive mechanism is consistent with the co-supporting cycle of Toh & Itano (2005). In addition, in the sense that small-scales play a role in organizing the roll-cell modes, our result is similar to McKeon & Sharma (2010) in which the most energetic mode in the presence of forcing by other smaller modes is a VLSM.

However, it should be noted that roll-cell modes constructed using LSM wavelengths are different to the roll-cells associated with VLSM wavelengths. When counter-rotating roll-cells are visualized using LSM wavelengths based on POD modes and linearly estimated conditional fields in the cross-stream plane (not shown here), the local, but strong sweep event was observed on a region beneath the event location $y/R = 0.15$, not on the near-wall region, implying less influence of LSMs on the near-wall regions.

Figure 21 shows superimposed correlation patterns R_{vl} and R_l using the artificially generated five energetic VLSM modes. Here, each correlation pattern of R_{vl} and R_l constructed from each VLSM mode (for example, R_{vl} and R_l from the 4th mode in figure 18) is simply summed with multiplying DNS-based eigenvalues through all five modes according to (5.4). Compared to figure 14(*b*), the difference is that the five VLSM patterns here are constructed by the alignments of the artificial LSMs that are either streamwise-aligned or spanwise-inclined, whereas there are no imposed LSM wavelengths in figure 14(*b*). As a result, an additional correlation pattern for R_l created by the alignments of the packet model is introduced in figure 21(*b*) by the spatial filtering of the artificial VLSM patterns. Since the synthetic VLSM patterns are constructed based on the POD modes using the present DNS data shown in figure 14, the overall correlation pattern R_{vl} in figure 21(*a*) is in excellent agreement with figure 14.

In figure 21(*b*), it is evident that the combination of the LSM patterns constructed for the formation of the several VLSM modes also induce a distinctive X-shaped pattern of R_l created by positive and negative correlation regions with a large helical angle $\beta_l \approx 25°$ at $y_{ref}/R = 0.15$, consistent with the pattern in figure 12(*b*). As shown in figure 17, such pattern of R_l is created by another periodic pattern of the LSMs,

compared to the alignment of the LSMs along the lines of the VLSMs. Note that the positive correlation region in the reference location is observed to be longer and wider than the real pattern of R_l in figure 12 due to the absence of small-scales motions in the model.

The pattern of the LSMs is consistent with a 3-D visualization study of a scalar field using dye slots in a low Reynolds number boundary layer (Delo, Kelso & Smits 2004). By examining the spanwise organization pattern of a large-scale packet structure (here, the term packet is used to describe regions of brightly marked dye within the boundary layer), in particular focusing on the outer portion of the boundary layer due to a clear pattern of the structure at that height without the complexity of higher levels, they identified that the LSMs in the outer layer ($y/R = 1.12$) are organized along diagonal lines, inclined to the streamwise direction within the range of approximately $-45°$ to $45°$. Compared to our result, the inclination angle $45°$ in the outer part of the boundary layer is larger than the angle in the outermost height in figure 13(*b*) owing to a different flow type with geometric contraction in the pipe core. The smaller helical angle when approaching the near-wall region in figure 13(*b*) is also consistent with the behaviour in Delo *et al.* (2004) in which they showed no strong diagonal orientation in the near-wall region. The formation pattern for R_l in figures 17 and 21 indicates that the increase of the helical angle for the LSMs along y/R is closely associated with the spanwise length scale growth of the structures, although the decrease of the spanwise domain size can cause the decrease of the helical angle, similar to that for the VLSMs in figures 11 and 13. However, since a helical angle β_{vl} for the VLSMs is created by an attached VLSM, similar to that in figure 17(*a*), the influence of the spanwise scale growth on β_{vl} is negligible.

Similarly, the described formation patterns for VLSMs and LSMs can provide an explanation for the different features of the spanwise-offset regions between them in figures 10–12. Since the streamwise-aligned VLSMs with a helical angle β_{vl} are attached to the wall by the role of the roll-cells at all y/R, the VLSM pattern with azimuthal-offset positive correlation regions can maintain an azimuthal similarity at $\sim 140°$ and $\sim 220°$ in a statistical sense with little influence of the spanwise scale growth along y/R (figures 10, 11, 15 and 17). However, since the LSMs in the outer layer are largely affected by the spanwise scale growth of the LSMs along y/R (figures 10 and 17), the azimuthal location of the spanwise-offset regions might be dependent of the radial position of the event. Furthermore, the smaller spanwise width of the LSMs rather than the VLSMs (figure 10) suggests that the offset regions can further persist up to $y/R = 0.5$ rather than the VLSM.

The spatial organization pattern observed in the present study is also consistent with a very recent experimental result in a turbulent boundary layer flow by Kevin *et al.* (2019). They investigated the spatial organization pattern of large-scale streaks without separation between LSMs and VLSMs, and observed that the large-scale coherence becomes increasingly misaligned with the distance from the wall (e.g. oblique/diagonal coherence inclined at $\pm 45°$ at around $y/R = 1.0$) with increasing meandering behaviour, similar to those in the earlier studies of Sillero, Jiménez & Moser (2014) and De Silva *et al.* (2018). They also found dominant streamwise-repeating behaviour of the large-scale structures. The overall organization pattern observed by Kevin *et al.* (2019) is very similar to our correlation patterns of R_l in which the helical angle increases with the distance from the wall with dominant anti-correlated regions fore-and-aft and side-to-side with respect to the reference position. The presence of the larger helical angle of the LSMs with the distance from the wall implies that the streamwise-aligned LSMs without spanwise-offset play an important role in creating

the correlation pattern of the VLSMs with small helical angle near the centreline (figures 11 and 13), and another periodic pattern of the LSMs compared to the alignment of the LSMs along the lines of the VLSMs leads to a larger helical pattern (figure 19).

6. Summary and conclusions

We analysed the DNS data of the fully developed turbulent pipe flow to investigate not only the formation mechanism of the VLSM from the LSMs but also the spatial organization patterns of the VLSMs and the LSMs with their statistical properties. The friction Reynolds number was $Re_\tau = 934$ and the streamwise domain length was $30R$ (Lee & Sung 2013). Consistent with the previous conjecture of Kim & Adrian (1999), the streamwise structure of the very large scale was found to be created by the coherent alignment of the LSM packets. The streamwise length and the helical angle of the VLSM were determined by the initial pattern (or alignment) of the LSMs, and the roll-cell-like motions might play an important role in organizing the alignment of the LSMs in a helical angle. This merging process between the LSMs was attributed to the continuous stretching and shearing of the hairpin packets of the LSMs due to wall-normal mean velocity gradient. The similarity of this elongation-concatenation mechanism and the mechanism found in turbulent boundary layer and channel flows (Lee & Sung 2011; Lee *et al.* 2014) indicates that formation of VLSMs by elongation-concatenation with spanwise angle does not depend fundamentally on the flow type.

The spectral filtration of the auto-correlations of the streamwise velocity fluctuations based on the cutoff streamwise wavenumber $k_xR = 2$ provided the statistical organization patterns and statistical properties of the VLSMs and LSMs, respectively. As similar to previous studies based on R_{uu} with low contour level, the correlation R_{vl} for the VLSMs showed that the dominant anti-correlated region to the positive correlation near the event point is located in the spanwise-offset region, and the VLSMs are attached to the wall even in the outer layer, indicating significant contribution of the VLSMs to the interaction of the structures between near-wall region and outer layer. On the other hand, examination of the spatial pattern of the LSMs revealed that the dominant anti-correlated regions of the streamwise velocity fluctuating structure exist fore-and-aft and side-to-side of the positive correlation region with the comparable size. The mean inclination angles of the VLSM and LSM to the wall in the logarithmic layer were approximately 4° and 20°, respectively, and this is distinguishable from the previous one (10°–15°) for a ramp-like low-momentum region by a hairpin packet due to global averaging of all structures.

The analysis using the artificially constructed hairpin packets based on the POD analysis showed that the highly elongated correlation of the VLSMs with the shallow angled X-shape pattern in the logarithmic layer (figures 11*b* and 14*a*) can be constructed by the superposition of very long structures composed of spanwise-offset LSMs aligned in the streamwise direction. The appearance of the meandering of the VLSM previously reported was successfully created by the alignment of the relatively straight spanwise-offset LSMs. In addition, the complex pattern of the streamwise- and spanwise-offset positive regions found in the correlations was also constructed using the combination of the synthetic VLSM patterns. This indicates that the correlation patterns shown in the DNS data are a consequence of spanwise-offset LSMs along a helical direction rather than a dominant very long sinusoidally wavering motion. The correlation pattern of the LSMs with the larger helical angles (figure 12*b*) rather than the VLSMs was induced by another periodic combination of the LSMs that are involved in creation of the VLSMs.

One school of thought attributes the creation of roll-cells to dynamic instability mechanisms that are not dependent on the formation of large hairpin packets (LSMs). For example, del Álamo & Jiménez (2006) found a linear instability mechanism in channels whose most-amplified wave solution has the form of roll-cells. Another school explains roll-cells as the response of those long, helical mode shapes that are most strongly amplified in the presence of forcing by smaller modes present in the (pipe) flow (McKeon & Sharma 2010). This mechanism allows for the possibility that large hairpin packets may be the smaller scales that force dynamic growth of the roll-cell modes. In opposition to these dynamic explanations, the POD analysis of the artificially generated VLSMs in the present study revealed that a roll-cell-like motion could be created by the VLSMs that are collectively constructed by the concatenation of the LSMs. The roll-cells were just dynamically passive kinematic manifestations of aligned packets being projected onto the POD modes. That is, averaging the flow around a set of (somehow) aligned packets creates a pattern that looks like a roll-cell when projected onto Fourier modes. However, the roll-cells centred in the outer layer were found to sweep the small-scale motions beneath the VLSM pattern, creating the small-scale footprint of the outer layer VLSM in the near-wall region. If the small-scale motions beneath the roll-cell motions can ultimately grow into LSM packets via auto-generation, the LSMs aligned closely enough to encounter each other can grow to a VLSM by a merging process (figures 2–4), finally intensifying the roll-cell. The LSM packets can align in a helical manner or in a straight manner, and the alignment of the LSMs with a helical angle is determined by the initial pattern of the LSMs prior to merger.

Interestingly, our generation process of the roll-cells shares some similarity with a secondary flow generation mechanism over a longitudinal surface roughness in a turbulent boundary layer. When the longitudinal surface roughness is presented on the bottom surface, it retards the local fluid directly over the elevated roughness elements due to large wall shear stress (thus, a low-momentum region), and a high-momentum region occurs in the valleys between the elevated roughness elements. In order to preserve mean flow continuity, a spanwise motion should be developed over the roughness, thus resulting in a large-scale counter-rotating circulation (i.e. roll-cells) (Vanderwel & Ganapathisubramani 2015; Hwang & Lee 2018). In the present study, the alignment of LSMs along a helical angle induces large Reynolds shear stress (wall shear stress) beneath the hairpins by the cooperative transfer of momentum between the hairpins (i.e. coherent stress) (Adrian *et al.* 2000). Thus, the VLSM inclined at an angle to the wall retards the local fluid in a similar way to the effects of the surface roughness, and generates a secondary flow-like pattern to preserve the conservation of mass, organizing the entire flow field far from the wall.

Acknowledgements

This work was supported by the National Research Foundation of Korea (NRF-2017R1D1A1A09000537, 2019R1A2C1083858) and US National Science Foundation Grant (CBET-0933848 and CBET-1335731).

REFERENCES

Adrian, R. J., Balachandar, S. & Liu, Z. C. 2001 Spanwise growth of vortex structure in wall turbulence. *KSME Intl J.* **15**, 1741–1749.

Adrian, R. J., Meinhart, C. D. & Tomkins, C. D. 2000 Vortex organization in the outer region of the turbulent boundary layer. *J. Fluid Mech.* **422**, 1–54.

ADRIAN, R. J. 2007 Hairpin vortex organization in wall turbulence. *Phys. Fluids* **19**, 041301.

DEL ÁLAMO, J. C. & JIMÉNEZ, J. 2006 Linear energy amplification in turbulent channels. *J. Fluid Mech.* **559**, 205–213.

DEL ÁLAMO, J. C. & JIMÉNEZ, J. 2009 Estimation of turbulent convection velocities and corrections to Taylor's approximation. *J. Fluid Mech.* **640**, 5–26.

BAILEY, S. C. C., HULTMARK, M., SMITS, A. J. & SCHULTZ, M. P. 2008 Azimuthal structure of turbulence in high Reynolds number pipe flow. *J. Fluid Mech.* **615**, 121–138.

BAILEY, S. C. C. & SMITS, A. J. 2010 Experimental investigation of the structure of large- and very-large-scale motions in turbulent pipe flow. *J. Fluid Mech.* **651**, 339–356.

BALAKUMAR, B. J. & ADRIAN, R. J. 2007 Large- and very-large-scale motions in channel and boundary-layer flows. *Phil. Trans. R. Soc. Lond.* A **365**, 665–681.

BALTZER, J. R. 2012 Structure and proper orthogonal decomposition in simulations of wall-bounded turbulent shear flows with canonical geometries. PhD thesis, Arizona State University.

BALTZER, J. R., ADRIAN, R. J. & WU, X. 2013 Structural organization of large and very-large scales in turbulent pipe flow simulation. *J. Fluid Mech.* **720**, 236–279.

BROWN, G. L. & THOMAS, A. S. W. 1977 Large structure in a turbulent boundary layer. *Phys. Fluids* **20**, S243.

BULLOCK, K. J., COOPER, R. E. & ABERNATHY, F. H. 1978 Structural similarity in radial correlations and spectra of longitudinal velocity fluctuations in pipe flow. *J. Fluid Mech.* **88**, 585–608.

CHRISTENSEN, K. T. & ADRIAN, R. J. 2001 Statistical evidence of hairpin vortex packets in wall turbulence. *J. Fluid Mech.* **431**, 433–443.

CHUNG, D. & MCKEON, B. J. 2010 Large-eddy simulation of large-scale structures in long channel flow. *J. Fluid Mech.* **661**, 341–364.

DELO, C. J., KELSO, R. M. & SMITS, A. J. 2004 Three-dimensional structure of a low-Reynolds-number turbulent boundary layer. *J. Fluid Mech.* **512**, 47–83.

DENNIS, D. J. C. & NICKELS, T. B. 2011 Experimental measurement of large-scale three-dimensional structures in a turbulent boundary layer. Part 2. Long structures. *J. Fluid Mech.* **673**, 218–244.

DE SILVA, C. M., KEVIN, B. R., HUTCHINS, N. & MARUSIC, I. 2018 Large coherence of spanwise velocity in turbulent boundary layers. *J. Fluid Mech.* **847**, 161–185.

DUGGLEBY, A., BALL, K. S., PAUL, M. R. & FISCHER, P. F. 2007 Dynamical eigenfunction decomposition of turbulent pipe flow. *J. Turbul.* **8** (43), 1–24.

FALCO, R. E. 1977 Coherent motions in the outer region of a turbulent boundary layers. *Phys. Fluids* **20**, S124.

GANAPATHISUBRAMANI, B., LONGMIRE, E. K. & MARUSIC, I. 2003 Characteristics of vortex packets in turbulent boundary layers. *J. Fluid Mech.* **478**, 35–46.

GUALA, M., HOMMEMA, S. E. & ADRIAN, R. J. 2006 Large-scale and very-large-scale motions in turbulent pipe flow. *J. Fluid Mech.* **554**, 521–542.

HELLSTRÖM, L. H. O., SINHA, A. & SMITS, A. J. 2011 Visualizing the very-large-scale motions in turbulent pipe flow. *Phys. Fluids* **23**, 011703.

HITES, M. H. 1997 Scaling of high-Reynolds number turbulent boundary layers in the national diagnostic facility. PhD thesis, Illinois Institute of Technology.

HOLMES, P., LUMLEY, J. L., BERKOOZ, G. & ROWLEY, C. W. 2012 *Turbulence, Coherent Structures, Dynamical Systems and Symmetry*, 2nd edn. Cambridge University Press.

HUTCHINS, N. & MARUSIC, I. 2007*a* Evidence of very long meandering features in the logarithmic region of turbulent boundary layers. *J. Fluid Mech.* **579**, 1–28.

HUTCHINS, N. & MARUSIC, I. 2007*b* Large-scale influences in near-wall turbulence. *Phil. Trans. R. Soc. Lond.* A **365**, 647–664.

HWANG, J., LEE, J. & SUNG, H. J. 2016 Inner–outer interaction of large-scale structures in turbulent channel flow. *J. Fluid Mech.* **790**, 128–157.

HWANG, Y. & COSSU, C. 2010 Self-sustained process at large scales in turbulent channel flow. *Phys. Rev. Lett.* **105**, 044505.

HWANG, H. G. & LEE, J. H. 2018 Secondary flows in turbulent boundary layers over longitudinal surface roughness. *Phys. Rev. Fluids* **3**, 014608.

KEVIN, MONTY, J. & HUTCHINS, N. 2019 The meandering behavior of large-scale structures in turbulent boundary layers. *J. Fluid Mech.* **865**, R1.

KIM, K. C. & ADRIAN, R. J. 1999 Very large-scale motion in the outer layer. *Phys. Fluids* **11**, 417–422.

KOVASZNAY, L. S. G., KIBENS, V. & BLACKWELDER, R. F. 1970 Large scale motion in the intermittent region of a turbulent boundary layer. *J. Fluid Mech.* **41**, 283–325.

LEE, J., LEE, J. H., CHOI, J.-I. & SUNG, H. J. 2014 Spatial organization of large-and very-large-scale motions in a turbulent channel flow. *J. Fluid Mech.* **749**, 818–840.

LEE, J. H. 2017 Large-scale motions in turbulent boundary layers subjected to adverse pressure gradients. *J. Fluid Mech.* **810**, 323–361.

LEE, J. H. & SUNG, H. J. 2011 Very-large-scale motions in a turbulent boundary layer. *J. Fluid Mech.* **673**, 80–120.

LEE, J. H. & SUNG, H. J. 2013 Comparison of very-large-scale motions of turbulent pipe and boundary layer simulations. *Phys. Fluids* **25**, 045103.

LEE, J. H., KWON, Y. S., HUTCHINS, N. & MONTY, J. P. 2012 Spatially developing turbulent boundary layer on a flat plate. *Bull. Am. Phys. Soc.* **57** arXiv:1210.3881.

LIU, Z.-C., ADRIAN, R. J. & HANRATTY, T. J. 2001 Large-scale modes of turbulent channel flow: transport and structure. *J. Fluid Mech.* **448**, 53–80.

MARUSIC, I. & ADRIAN, R. J. 2012 Coherent structures in flow over hydraulic engineering surfaces. *J. Hydraul. Res.* **50** (5), 451–464.

MARUSIC, I. & HUTCHINS, N. 2008 Study of the log-layer structure in wall turbulence over a very large range of Reynolds number. *Flow Turbul. Combust.* **81**, 115–130.

MARUSIC, I., MCKEON, B. J., MONKEWITZ, P. A., NAGIB, H. M., SMITS, A. J. & SREENIVASAN, K. R. 2010 Wall-bounded turbulent flows at high Reynolds numbers: recent advances and key issues. *Phys. Fluids* **22**, 065103.

MARUSIC, I. & MONTY, J. P. 2019 Attached eddy model of wall turbulence. *Annu. Rev. Fluid Mech.* **51**, 49–74.

MATHIS, R., HUTCHINS, N. & MARUSIC, I. 2009 Large-scale amplitude modulation of the small-scale structures in turbulent boundary layers. *J. Fluid Mech.* **628**, 311–337.

MCKEON, B. J. & SHARMA, A. S. 2010 A critical-layer framework for turbulent pipe flow. *J. Fluid Mech.* **628**, 311–337.

MEINHART, C. D. & ADRIAN, R. J. 1995 On the existence of uniform momentum zones in a turbulent boundary layer. *Phys. Fluids* **7**, 694–696.

MONTY, J. P., STEWART, J. A., WILLIAMS, R. C. & CHONG, M. S. 2007 Large-scale features in turbulent pipe and channel flows. *J. Fluid Mech.* **589**, 147–156.

MONTY, J. P., HUTCHINS, N., NG, H. C. H., MARUSIC, I. & CHONG, M. S. 2009 A comparison of turbulent pipe, channel and boundary layer flows. *J. Fluid Mech.* **632**, 431–442.

PERRY, A. E. & CHONG, M. S. 1982 On the mechanism of wall turbulence. *J. Fluid Mech.* **119**, 173–217.

PERRY, A. E. & MARUSIC, I. 1995 A wall-wake model for the turbulence structure of boundary layers. Part 1. Extension of the attached eddy hypothesis. *J. Fluid Mech.* **298**, 361–388.

PRIYMAK, V. G. & MIYAZAKI, T. 1994 Long-wave motions in turbulent shear flows. *Phys. Fluids* **6**, 3454–3464.

SILLERO, J. A., JIMÉNEZ, J. & MOSER, R. D. 2014 Two-point statistics for turbulent boundary layers and channels at Reynolds numbers up to $\delta^+ \approx 2000$. *Phys. Fluids* **26** (10), 105109.

TOH, S. & ITANO, T. 2005 Interaction between a large-scale structure and near-wall structures in channel flow. *J. Fluid Mech.* **524**, 249–262.

TOMKINS, C. D. & ADRIAN, R. J. 2003 Spanwise structure and scale growth in turbulent boundary layers. *J. Fluid Mech.* **490**, 37–74.

TOWNSEND, A. A. 1976 *The Structure of Turbulent Shear Flow*, 2nd edn. Cambridge University Press.

VANDERWEL, C. & GANAPATHISUBRAMANI, B. 2015 Effects of spanwise spacing on large-scale secondary flows in rough-wall turbulent boundary layers. *J. Fluid Mech.* **774**, R2.

WU, X., BALTZER, J. R. & ADRIAN, R. J. 2012 Direct numerical simulation of a $30R$ long turbulent pipe flow at $R^+ = 685$: large- and very large-scale motions. *J. Fluid Mech.* **698**, 235–281.

ZHOU, J., ADRIAN, R. J., BALACHANDAR, S. & KENDALL, T. M. 1999 Mechanisms for generating coherent packets of hairpin vortices. *J. Fluid Mech.* **387**, 353–396.